TU Delft

Delft University of Technology

Document Version
Final published version

Licence
Dutch Copyright Act (Article 25fa)

Citation (APA)
Hunter, T. P., Avallone, F., Doan, N. A. K., & Ragni, D. (2026). Characterization of Communicating Turbulent Grazing Flows Through a Resolved Porous Medium. *Flow, Turbulence and Combustion*, *116*(1), Article 10. https://doi.org/10.1007/s10494-025-00711-1

Important note
To cite this publication, please use the final published version (if applicable).
Please check the document version above.

Copyright
In case the licence states “Dutch Copyright Act (Article 25fa)”, this publication was made available Green Open Access via the TU Delft Institutional Repository pursuant to Dutch Copyright Act (Article 25fa, the Taverne amendment). This provision does not affect copyright ownership.
Unless copyright is transferred by contract or statute, it remains with the copyright holder.

Sharing and reuse
Other than for strictly personal use, it is not permitted to download, forward or distribute the text or part of it, without the consent of the author(s) and/or copyright holder(s), unless the work is under an open content license such as Creative Commons.

Takedown policy
Please contact us and provide details if you believe this document breaches copyrights.
We will remove access to the work immediately and investigate your claim.

*This work is downloaded from Delft University of Technology.*

Flow, Turbulence and Combustion (2026) 116:10
https://doi.org/10.1007/s10494-025-00711-1

RESEARCH

# Characterization of Communicating Turbulent Grazing Flows Through a Resolved Porous Medium

**Thomas P. Hunter[1] · Francesco Avallone[2] · Nguyen Anh Khoa Doan[1] · Daniele Ragni[1]**

Received: 11 June 2025 / Accepted: 25 September 2025 / Published online: 2 December 2025
© The Author(s), under exclusive licence to Springer Nature B.V. 2025

**Abstract**
Porous media are a promising technology to reduce turbulent boundary layer trailing edge noise. However, the fact that the porous material is grazed by turbulent flow on both sides makes its characterization not trivial. This paper describes the modifications resulting from the interaction between the grazing flows through the porous medium, defined as communication. To this end, lattice-Boltzmann simulations of two communicating turbulent channel flows separated by a fully resolved porous medium are carried out. The porous medium is realized as a 75% porous triply periodic minimal surface of type Schwarz' P. Results are compared against the case with porous medium backed by a solid wall and the smooth wall channel flow. When communication between the two channel flows is allowed, spanwise coherent structures appear that are assimilated to a shear instability at a non-dimensional frequency of $St_t = 0.02$. Instantaneous flow through the porous medium is observed and is driven by a time-dependent pressure differential between the channels (with a zero mean and 7.8 Pa standard deviation). This leads to a decrease in energy in turbulent scales smaller than $2.5\delta$ and for bulk scaled frequencies greater than $St_b = 0.41$. These flow modifications are not observed in the non-communicating case, with the wall preventing flow through, where the topology of the fluctuating statistics is similar to the smooth wall case. Finally, the drag is found to increase by over 200% with respect to the non-communicating case and 650% with respect to a smooth turbulent channel flow. The drag increase is found to be driven by the velocity fluctuations impinging on the porous topology. The communication does not follow the asymptotic drag relation for the same equivalent roughness, thus entering a different drag regime.

**Keywords** Trailing edge noise · Porous media · Communicating grazing flows · Wall turbulence

Francesco Avallone, Nguyen Anh Khoa Doan and Daniele Ragni contributed equally to this work.

Extended author information available on the last page of the article

## 1 Introduction

Trailing-edge noise (Brooks et al. 1989) can be mitigated by various means, such as trailing-edge serrations (Jones and Sandberg 2012). In recent times, porous trailing edges were considered due to their large noise reduction potential in a wider range of operating conditions with respect to state-of-the-art serrations (Lee et al. 2021; Zhou et al. 2022). Similarly to serrated trailing edges, they are less effective when the airfoil generates lift (Herr et al. 2014; Teruna et al. 2021). Porous trailing edges have also been found to induce a high-frequency acoustic signature, attributed to the impact of roughness (Ye et al. 2019). Porous trailing edges enable hydrodynamic communication between the pressure and suction side of the airfoil, providing a milder transition between the solid airfoil and the wake (Geyer et al. 2009), referred to as the pressure release mechanism (Herr et al. 2014). The communication between the two boundary layers was quickly identified as a necessary condition and the largest driver for noise reduction, independent of the specific porous medium being used (Geyer et al. 2009), as significant noise reduction was achieved for most porous media tested (Lee et al. 2021). Porous media are characterized through their steady properties, relating a pressure drop and a mass flow rate, despite the operating conditions being unsteady and the properties depending on the thickness. When modeling porous trailing edges using the Forchheimer corrected Darcy law, permeability was identified as the key material property related to noise reduction, while tortuosity (Rubio Carpio et al. 2020), and the non-linear permeability (Luesutthiviboon et al. 2021) play a significant but more limited role. Despite previous research on porous trailing edges, both numerical (Teruna et al. 2021) and experimental (Rubio Carpio et al. 2019), the modifications induced by the communication of grazing flows through porous media remains largely unexplored due to the complex flow conditions. The characterization of a communicating regime is further complicated by the difficulty in characterizing porous media [Marcus 1962; Tjaden et al. 2018; Aghaei-Jouybari et al. 2024 ], in particular when it is thin (Baril et al. 2008; Teruna et al. 2021). The goal of this paper is to systematically characterize the modifications occurring in interacting turbulent grazing flows through porous media, herein referred to as communication. The two main contributions are thus a novel setup, and a quantitative analysis of the communicating regime. First, we propose and use a dedicated numerical setup based on turbulent channel flows communicating through a pore-resolved porous medium. The definition of the medium is provided analytically and the setup allows for controlled flow conditions. Second, the aerodynamic performance is quantified and decomposed into pressure and friction drag contributions, and the turbulence modifications are related to the modifications of the pressure and velocity fields. For this purpose, the communicating case is compared to two control cases considered in the rest of the paper: a smooth impermeable walled channel flow, and a channel flow over the same porous medium backed with a solid wall preventing the channels from interacting.

## 2 Methodology

### 2.1 Flow Solver

The numerical setup described previously was simulated using the commercial software PowerFLOW 6–2021, which relies on the Lattice Boltzmann Method (LBM). This computational method has been employed in previous research that focused on predicting and reducing turbulent boundary layer - trailing edge noise (Teruna et al. 2021; Avallone et al. 2018). The LBM characterizes the movement of fluid particles on a smaller, mesoscopic scale and monitors how these particles are transported and interact through distribution functions aligned with a set number of predefined directions. The procedures are described by the LB equation, as shown below:

$$\frac{\partial F}{\partial t} + \mathbf{V} \cdot \nabla F = \mathbf{C}, \tag{1}$$

where $F(\mathbf{x}, t)$ represents the particle distribution function in both spatial ($\mathbf{x}$) and temporal ($t$) dimensions, $\mathbf{V}$ the particle velocity, and $\mathbf{C}$ the collision operator. To discretise Eq. 1, 19 vectors in three-dimensional spatial space (known as D3Q19) are employed, incorporating a third-order truncation of the Chapman-Enskog equation. This method has been demonstrated to accurately approximate the Navier-Stokes equations for an ideal gas at low Mach numbers and under isothermal conditions (Chen et al. 1992). The particle distribution function is solved on a Cartesian grid, referred to as a lattice. The discretized form of the Lattice Boltzmann (LB) equation is expressed as follows:

$$F_n(\mathbf{x} + \mathbf{V}_n \Delta t, t + \Delta t) - F_n(\mathbf{x}, t) = \mathbf{C}_n(\mathbf{x}, t), \tag{2}$$

where $F_n$ is the particle distribution function along the $n$-th lattice direction, $\mathbf{V}_n$ is the discrete particle velocity in the $n$-th direction. The collision term $\mathbf{C}_n$ follows the Bhatnagar-Gross-Krook model (Bhatnagar et al. 1954):

$$\mathrm{C}_n = -\frac{\Delta t}{\tau}[F_n(\mathbf{x}, t) - F_n^{eq}(\mathbf{x}, t)], \tag{3}$$

where $\tau$ is the relaxation time, a function of fluid viscosity and temperature, and $F_n^{eq}$ is the equilibrium distribution function of Maxwell-Boltzmann that is approximated with a second-order expansion (Chen et al. 1992) as:

$$F_n^{eq} = \rho \omega_n \left[1 + \frac{\mathbf{V}_n \mathbf{u}}{a_s^2} + \frac{(\mathbf{V}_n \mathbf{u})^2}{2a_s^4} - \frac{|\mathbf{u}|^2}{2a_s^2}\right], \tag{4}$$

where $\omega_n$ are the fixed weight functions based on the D3Q19 model (Chen et al. 1992), and $a_s = 1/\sqrt{3}$ is the non-dimensional speed of sound in lattice units. Following the solution of Eq. 2 to obtain the distribution functions, macroscopic fluid characteristics, including density denoted as $\rho$ and velocity denoted as $\mathbf{u}$, are calculated by summing up the weighted distribution function across the state space.

$$\rho(\mathbf{x},t) = \sum_n F_n(\mathbf{x},t), \tag{5}$$

$$\rho\mathbf{u}(\mathbf{x},t) = \sum_n \mathbf{V}_n F_n(\mathbf{x},t). \tag{6}$$

The numerical solver uses the Very Large Eddy Simulation (VLES) method to account for the impact of turbulent scales that are not resolved on the sub-grid level. This approach incorporates an eddy viscosity model into the collision term of the LB equation (Teixeira 1998). In this specific implementation, a modified $k-\epsilon$ two-equation turbulence model, which relies on the renormalization group formulation, is applied. Turbulent fluctuations are modeled by substituting the relaxation time $\tau$ with an effective relaxation time denoted as $\tau_{eff}$.

$$\tau_{eff} = \tau + C_\mu \frac{k^2/\epsilon}{\sqrt{1+\eta^2}}, \tag{7}$$

where $C_\mu = 0.09$ and $\eta$ is a combination of the local strain $k|\mathrm{S}/\epsilon|$, local vorticity $k|\omega/\epsilon|$ and local helicity parameters (Chen et al. 2004). This ensures that nearly all turbulent structures are fully resolved following Pope's criterion (Pope 2000). The implementation of the turbulence modeling was validated in two ways: first in Appendix A, comparing the Turbulent Channel Flow (TCF) case to a Direct Numerical Simulation (DNS) dataset, and second in Appendix B, with a grid convergence looking at both the resolution of turbulence and the pore-resolved geometry. Furthermore, the numerical schemes associated with the solver ensure that all the relevant features of turbulence are resolved. Large-scale vortical structures are allowed to develop as the modified relaxation time aligns the LB solver to the characteristic time scales of the turbulent flow field. LBM solutions are unsteady and turbulent, conserving the history of the flow field. Moreover, it can be demonstrated through the Chapman-Enskog expansion that the model successfully captures the nonlinearity of the Reynolds stresses (Teixeira 1998; Chen et al. 2004).

The LBM-VLES approach differs significantly from the Reynolds-averaged Navier-Stokes (RANS) method, even though both approaches solve similar turbulence transport equations. In the case of RANS, the quantities derived from the turbulence model explicitly define the Reynolds stresses, which are integrated into the governing equations. However, in the LBM-VLES approach, these quantities are solely employed to modify the relaxation properties of the system in the collision step. The resulting modeled turbulent kinetic energy was computed to be less than 10% of the resolved turbulent kinetic energy throughout the domain; most turbulent scales are therefore resolved.

The cubic elements that form the lattice in the LB scheme are known as "voxels". The simulation domain is divided into volume refinement regions, each employing varying voxel resolutions. To represent solid boundaries,"surfels" or surface pixels are used, and they are generated at the points where voxels intersect with solid triangulated surfaces. The boundary condition applied to these walls determines how fluid particles interact in the collision term of the LB scheme. For instance, it involves a particle bounce-back process for a no-slip wall and a specular reflection for a slip wall (Chen et al. 1998). To further reduce computational costs in resolving the boundary layer, especially at high Reynolds numbers, a

wall model is applied to the first voxel (Teixeira 1998; Wilcox 2006). This model is rooted in the generalized law-of-the-wall model (Launder and Spalding 1983), which has been extended to account for the influence of pressure gradients.

### 2.2 Numerical Setup

The numerical setup, illustrated in Fig. 1, consists of two vertically stacked turbulent channel flows communicating through a porous medium. The simulation domain dimensions are $L_x \times L_y \times L_z = 6\delta \times (4\delta + t) \times 2\delta$, where $\delta$ is the half channel height, and $t = 0.4\delta$ the porous medium thickness. This allows to study the effect of variations in the porous medium design space (i.e. scale, porosity, thickness, etc.) and flow conditions (streamwise and wall-normal pressure gradients) on the aerodynamic performance of the considered porous flat plate.

Periodic boundary conditions are applied in the stream- and spanwise directions. The top and bottom channels are bound by the porous medium on one side and a smooth non-slip wall on the other. The flow is driven by a local forcing term, analogous to a pressure gradient in the streamwise direction, $\partial p/\partial x$.

The solutions were computed from an initial condition corresponding to a parabolic velocity profile superimposed with low frequency periodic velocity fluctuations $sin(\cdot)$, an order of magnitude smaller than the centerline velocity to facilitate transition. An initial simulation time of 10 to 20 viscous flow-throughs was used, until the spatially averaged streamwise velocity was within 10% of the mean.

### 2.3 Setup Verification

Two verification steps were performed, being: grid convergence and domain independence. The grid convergence, as shown in Appendix B, was used to determine the required resolution to capture both turbulence and the topology of the porous medium. A resolution of 32 voxels per reference length $L_{ref}$ was found to be necessary. The study of the length of the

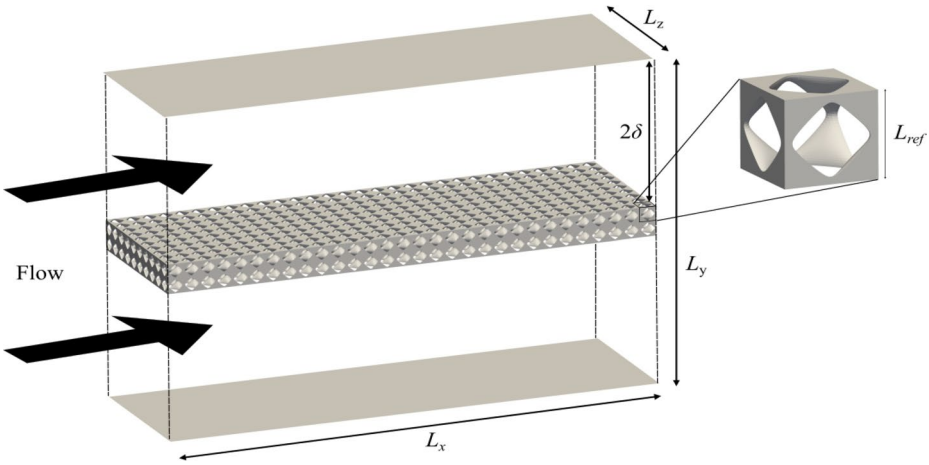



**Fig. 1** Schematic of the proposed communicating turbulent channel flows (C-TCF) and unit cell of the 75% porous TPMS Schwarz's P "primitive"

domain in the streamwise direction was necessary to ensure the domain independence of the results. The results of the analysis are presented in Appendix C and leads to a domain dimension of $L_x \times L_y \times L_z = 6\delta \times (4\delta + t) \times 2\delta$. The distribution of the voxel refinement levels is shown in Fig. 2.

Using this set-up and a pressure drop set-up, discussed in the following section, it was possible to show that the geometric fidelity of the pore resolution is the driving constraint to determine the grid refinement level. The grid convergence study shows a final mean wall resolution of $\Delta y^+ < 1$.

### 2.4 Porous Medium Definition

The chosen porous medium is the Triply Periodic Minimal Surface (TPMS) Schwarz's P ('Primitive') with 75% porosity. TPMS enable the parametric study of complex porous media due to their mathematical definitions relying on few parameters. These criteria were chosen to emulate similar properties to the metal foams whose noise reduction was documented (Herr et al. 2014; Rubio Carpio et al. 2020).

For a given closed curve in space, it can be shown that there exists a surface minimizing its surface area (Meeks 1990), as shown in Fig. 3(a). Assembling such a patch results in a specific surface that is triply periodic in space, resulting in a TPMS. The example for the TPMS Schwarz's P is shown in Fig. 3(b). Specifically, the subset of TPMS of interest is obtained through the following explicit relations (Gandy and Klinowski 2000):

$$\begin{aligned} x_1 &= \Lambda_1 Re\left(e^{i\theta}\int_{\omega_0}^{\omega}(1-\tau^2)R(\tau)\,d\tau\right), \\ x_2 &= \Lambda_2 Re\left(e^{i\theta}\int_{\omega_0}^{\omega}-i(1+\tau^2)R(\tau)\,d\tau\right), \\ x_3 &= \Lambda_3 Re\left(e^{i\theta}\int_{\omega_0}^{\omega}2\tau R(\tau)\,d\tau\right), \end{aligned} \tag{8}$$

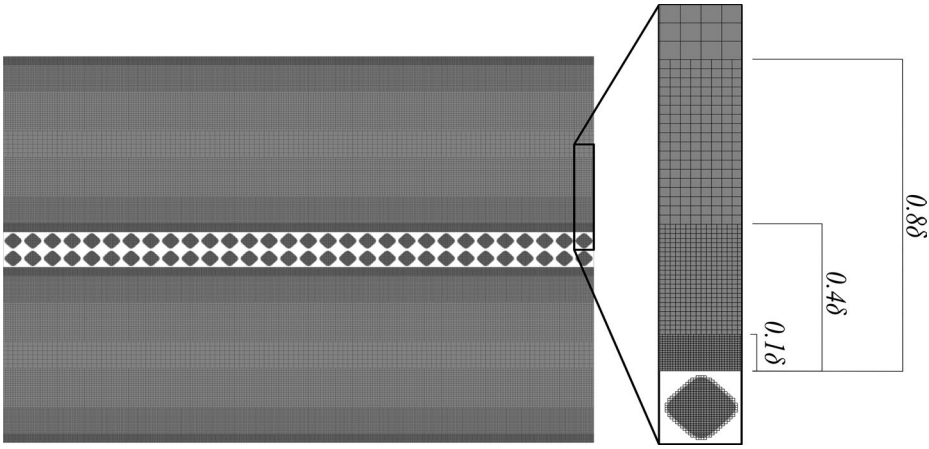



**Fig. 2** The proposed communicating channels setup in a span-normal slice illustrating the voxel distribution

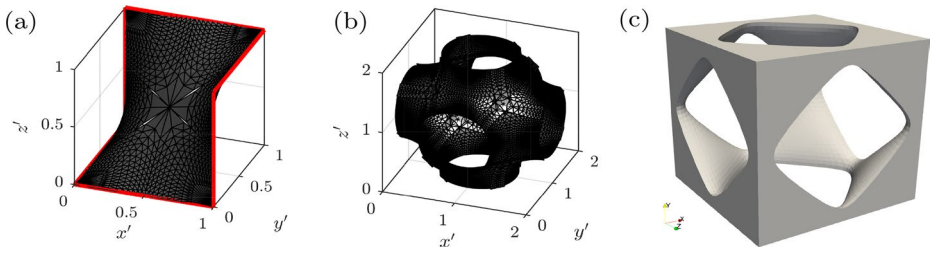



**Fig. 3** Construction of the TPMS Schwartz's P as shown through its (**a**) fundamental patch for TPMS Schwartz' D ('diamond', conjugate of P), (**b**) the assembled unit cell, and (**c**) the unit cell of P075

where $i^2 = -1$, $\Lambda_i$ the anisotropy and scaling vector, and $\tau = \tau_a + i\tau_b$ a point in the complex plane used to map with the Weierstrass function $R(\tau) = \frac{1}{\sqrt{\tau^8+\lambda\tau^4+1}}$, $\theta$ the Bonnet angle and $\lambda = -14$. The Weierstrass function enables the creation of a TPMS family that is described by its Bonnet angle and $\Lambda_i$. The coordinates are obtained by evaluating the real part ($Re(\cdot)$) of the integrals from some fixed points $\omega_0$ to a variable point $\omega$ in the complex plane. The surface, thus obtained, can be assembled to form a triply periodic surface (Gandy and Klinowski 2000). These surfaces can be approximated by the periodic nodal surface of a sum defined in terms of a Fourier series (Gandy et al. 2001).

$$\phi(\mathbf{r}) = \sum_{\mathbf{k}} F(\mathbf{k})\cos[\pi\mathbf{k}\cdot\mathbf{r} - \alpha(\mathbf{k})] = 0, \tag{9}$$

where $\mathbf{k}$ are the reciprocal lattice vectors, $\alpha(\mathbf{k})$ a phase shift, and $F(\mathbf{k})$ a given amplitude.

The TPMS Schwartz's P is approximated by truncating the series to its leading term in literature [Gandy et al. 2001; Schnering and Nesper, 1991; Feng et al. 2021; Piest et al. 2024 ], leading to the implicit relations for the TPMS P:

$$\cos(X) + \cos(Y) + \cos(Z) = \phi, \tag{10}$$

where $X$, $Y$, and $Z$ are respectively equal to $\Lambda_i 2\pi x_i / L_{ref}$, $\phi$=0.8644 is an iso-level controlling the porosity of the medium, and $L_{ref} = 2$ mm is the unit cell reference length. It must be noted that the surface is a TPMS only for $\phi$=0. This unit cell reference length and iso-level were chosen to obtain a ratio of pore diameter to boundary layer thickness $d_p/\delta \approx 17\%$. This ratio, as well as the porosity of 75%, was chosen as it is in the range of parameters that have been observed to lead to the largest noise reduction potential in Rubio Carpio et al. (Rubio Carpio et al. 2019). The corresponding unit cell for the TPMS Schwartz's P is shown in Fig. 3(c). In this study, the TPMS Schwartz's P with the parameters from Table 1 is referred to as **P075**.

The discrete geometries were obtained by generating triangulated iso-surfaces in MATLAB. They were given as input in 3DS PowerFLOW to fully resolve the porous medium. The geometry uses a resolution of $32^3$ nodes in each direction following from the accurate approximation of the local geometrical curvature (Gandy et al. 2001).

**Table 1** Geometric generation parameters of the TPMS unit cells considered

| Case | $L_{ref}/\delta$ | $\Lambda$ | $\theta$ |
|---|---|---|---|
| **P075** | 20% | (1, 1, 1) | $\pi/2$ |

**Table 2** Pressure drop simulation parameters

| Case | $t$ [m] | $\Delta y$ [m] | $v_D[m/s]$ | $\Delta p$ [Pa] | $T_{\text{avg}} v_D/t$ | $N_{\text{voxels}}$ [$\times 10^5$] |
|---|---|---|---|---|---|---|
| **P075**-$x_1$ | $20 \times 10^{-3}$ | $6.25 \times 10^{-5}$ | 0.4 | 4.15 | 11 | 5.7 |
| **P075**-$x_2$ | $20 \times 10^{-3}$ | $6.25 \times 10^{-5}$ | 0.8 | 10.56 | 11 | 5.7 |
| **P075**-$x_3$ | $20 \times 10^{-3}$ | $6.25 \times 10^{-5}$ | 1.0 | 14.56 | 11 | 5.7 |
| **P075**-$y_1$ | $4 \times 10^{-3}$ | $6.25 \times 10^{-5}$ | 0.4 | 1.44 | 55 | 3.2 |
| **P075**-$y_2$ | $4 \times 10^{-3}$ | $6.25 \times 10^{-5}$ | 0.8 | 4.29 | 55 | 3.2 |
| **P075**-$y_3$ | $4 \times 10^{-3}$ | $6.25 \times 10^{-5}$ | 1.0 | 6.25 | 55 | 3.2 |

## 2.5 Material Properties Characterization

In this study, the porous medium is modeled by the Forchheimer corrected Darcy law, as shown in Eq. 11. In this equation, $\Delta p$ is the pressure differential across the porous medium, $t$ is the material thickness, $\mu$ is the fluid dynamic viscosity, $\rho$ the fluid density, $v_D$ the Darcy velocity, $K_{ii}$ is the permeability along the $i$-th component and $C_{ii}$ the inertial permeability, also referred to as the form coefficient. The off-diagonal terms of the permeability tensors are zero since the flow and pressure gradient directions are coincident for the **P075**.

$$\frac{\Delta p_i}{t} = \frac{\mu}{K_{ii}} v_{D,i} + \rho C_{ii} v_{D,i}^2. \tag{11}$$

Thin porous media differ in their behaviour from thick porous media ($t > 10d_p$) as the material properties show a dependency on the thickness. The chosen **P075** is expected to behave like a thin porous medium in the wall-normal direction following the observations in both material science (Baril et al. 2008) and previous work on porous trailing edges (Rubio Carpio et al. 2020; Teruna et al. 2021). In the spanwise and streamwise directions, the porous medium behaves as a thick porous medium, in part due to the periodic boundary conditions used. It was therefore chosen to characterize the porous media in this study using the thicknesses $t = 2L_{ref}$, and $t = 10L_{ref}$ for both the wall-normal and other directions respectively, using the simulation parameters from Table 2. The permeability $K_{ij}$ and the inertial permeability $C_{ij}$ are both tensors. However, to the author's knowledge, there currently does not exist a framework to determine the off-diagonal terms of thin porous media since the impact of entrance and exit effects becomes significant, as is discussed below. Current literature allows for the determination of the off-diagonal terms (Aghaei-Jouybari et al. 2024), however, the latter study neglects entrance and exit effects on the diagonal and off-diagonal terms. The current model does account for anisotropy since the streamwise (thick) and wall-normal (thin) are allowed to take different values.

The pressure drop was measured numerically with the same flow solver as the channel flow simulations by computing the difference in pressure between the inlet and the outlet, as shown in Fig. 4. The total distance over which the pressure drop is approximately $\Delta x > 10 \times t$. The domain size used is $(50mm + t + 50mm) \times 3L_{ref} \times 3L_{ref}$. This was

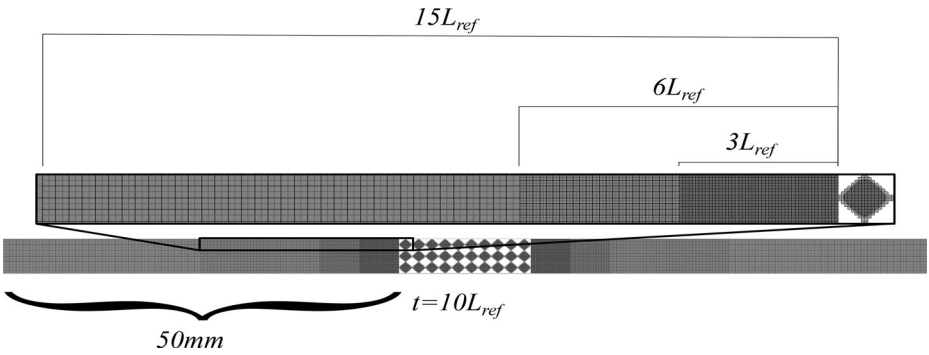



**Fig. 4** Pressure drop setup and voxel refinement distribution for the thick sample ($t = 10L_{ref}$) of P075

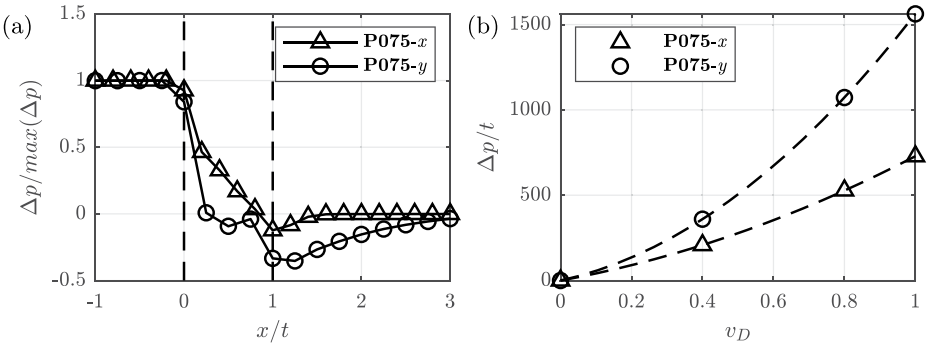



**Fig. 5** (**a**) Pressure recovery profile in the streamwise direction, and (**b**) comparison of the curve fitting for $t = 2L_{ref}$ and $t = 10Lref$

done as there is evidence that measuring the pressure in the vicinity of the porous medium (Aghaei-Jouybari et al. 2024; Asbai-Ghoudan et al. 2021) underestimates the pressure drop significantly for thin porous media, with inertial effects playing a large role in the pressure recovery and total pressure drop. This is further confirmed by the observation of the pressure field in Fig. 5(a). Since the pressure in the vicinity of the porous medium is still recovering and adapting, the pressure drop would be underestimated by over 10% for this particular case. The error would be larger for higher Darcy velocities relative to the thickness of the porous medium. This discrepancy may appear small but would compound to give erroneous measurements of permeability and non-linear permeability.

Both linear and non-linear permeability are then computed by performing a quadratic fit through the obtained points of pressure drop. The resulting measured permeabilities and inertial permeabilities, as well as the simulation and fitting parameters, are summarised in Table 3. The quality of the quadratic fit can be seen in Fig. 5(b).

## 2.6 Test Cases

The simulations are divided into three test cases: the smooth wall case (**S**), the communicating case with the same flow conditions in both channels (**C**), and the blocked case (**B**)

**Table 3** Pressure drop simulation results, where $r_i^2$ denotes the coefficient of determination of the quadratic fit. Note: the $x$-axis (streamwise) is for $t = 10L_{ref}$ and $y$-axis (wall-normal) for $t = 2L_{ref}$

| Geometry | $K_{xx}\,[m^2]$ | $C_{xx}\,[1/m]$ | $r_x^2$ | $K_{yy}\,[m^2]$ | $C_{yy}\,[1/m]$ | $r_y^2$ |
|---|---|---|---|---|---|---|
| **P075** | $4.70 \times 10^{-8}$ | 284 | 1 | $3.93 \times 10^{-8}$ | 904 | 1 |

**Table 4** Summary of the simulations of this study

| Case | $\Delta y$ [m] | $N_{voxels}$ [$\times 10^6$] | max($y^+$\|wall) | F [$mN$] | $Re_b$ | $Re_\tau$ | $L_{ref}^+ \approx d^+$ | $\frac{T_{avg} u_\tau}{\delta}$ |
|---|---|---|---|---|---|---|---|---|
| **S** | $6.25 \times 10^{-5}$ | 17.7 | 1.9 | 2.21 | $19.3 \times 10^3$ | 590 | - | 62 |
| **B**-LR (**B**) | $6.25 \times 10^{-5}$ | 22.1 | 0.85 | 2.21 | $15.3 \times 10^3$ | 633 | 127 | 27 |
| **B**-HR | $6.25 \times 10^{-5}$ | 22.1 | 1.17 | 4.58 | $22.3 \times 10^3$ | 911 | 182 | 39 |
| **bB** | $6.25 \times 10^{-5}$ | 26.5 | 0.67 | 2.21 | $15.0 \times 10^3$ | 639 | 128 | 29 |
| **C** | $6.25 \times 10^{-5}$ | 44.2 | 1.0 | 2.21 | $9.02 \times 10^3$ | 754 | 151 | 46 |

where the porous medium is present but lacking communication due to the presence of a wall at the center of the domain. Both cases **C** and **B** have the same forcing applied in the channels. Therefore, a difference in drag from the porous medium will result in variations in bulk and friction velocities. Additional sub-cases are proposed for the relevant analyses in the subsequent sections. Variations in forcing and friction Reynolds number are denoted with -LR and -HR corresponding to the lower and higher Reynolds number case. The forcing for both cases were chosen to be the same as the smooth wall forcing at $Re_\tau = 590$, and $Re_\tau = 850$. This was done to ensure that a sufficient log layer would be present. The case **B**-LR is used as a reference case for comparison throughout. A case with the communication being blocked at the bottom of the porous medium ($t = 2L_{ref}$) is denoted **bB**. Cases **B**-LR and **B**-HR are used to fit the proportionality coefficient between the non-linear permeability and an equivalent roughness height, used to relate material properties to the velocity deficit in Section 2.5. Moreover, they are used to highlight that differences in Reynolds numbers or porous thickness cannot be assimilated to the change of regime induced by the communication, as will be discussed subsequently. The simulation parameters are presented in Table 4.

The relevant non-dimensionalization and Reynolds numbers are used to perform the comparison between non- and communicating cases. Most parameters are viscous-scaled, as determined from the shift in the virtual origin of turbulence (Ibrahim et al. 2021), since the relative distribution of the Reynolds shear stress profile is unaltered across all cases. The local turbulent kinetic energy is used in the spectral analysis as a means to segregate the locality of the shedding-like turbulence and the global drag imparted by the porous medium.

## 3 Flow Field Description

The results obtained for the smooth-walled case **S**, the porous case **B** and communicating case **C** are presented in this section. The various instantaneous and mean fields are presented to qualitatively assess the flow field topology. Particular attention is given to the differences between the cases with and without communication. Further quantification of these modifications is presented in Sect. 4.

### 3.1 Instantaneous Flow Fields

Instantaneous snapshots for the solutions of cases **S**, **B**, and **C** are presented in Fig. 6. Videos of the simulations are available at the link in Sect. 5. In the figure, iso-surfaces of the $\lambda_2$ vortex criterion are given at a level of $-2 \times 10^7$ $[1/s^2]$. The iso-surfaces are coloured with the streamwise velocity.

The vortical structures in case **S**, as shown in Fig. 6(a), present the horseshoe vortices whose roll-up angle is associated with the friction velocity. Figures 6(b) and 6(c), corresponding to cases **B** and **C** respectively, show a modification of these vortical structures. Smaller vortical structures can be observed in the annotation of case **B**. However the anchor points of the horseshoe vortices appear to correspond to the inter-pore spacing, as shown in the figure. For case **C**, the vortical structures appear elongated in the wall-normal direction. They are then convected in the streamwise direction under the increase of streamwise velocity towards the center of the channel where they elongate. The streamwise velocity of the vortical structures is shown in the figure and illustrates a larger relative convection velocity in case **B** compared to case **S**. The increased relative convection velocity is a sign of increased mixing between the near-wall cycle, affected by the presence of the porous medium, and the far-wall cycle nearer the center of the channel (Shahzad et al. 2023). On the contrary, case **C** shows a decrease in the convection velocity of the vortical structures with larger low velocity regions. Additionally, in case **C**, the vortical structures are only intermittently present in the vicinity of the porous medium and in regions of low stream-

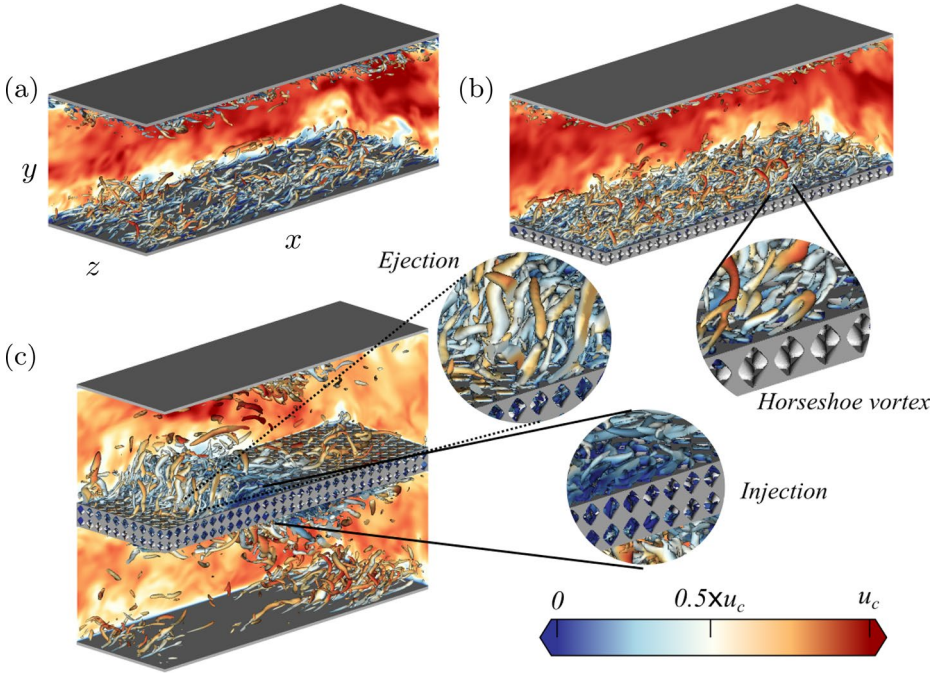



**Fig. 6** Instantaneous snapshots of $\lambda_2$ vortex identification criterion at an iso-value of $-2 \times 10^7$ $[1/s^2]$, coloured by streamwise velocity for (**a**) case S, (**b**) case B, and (**c**) case C

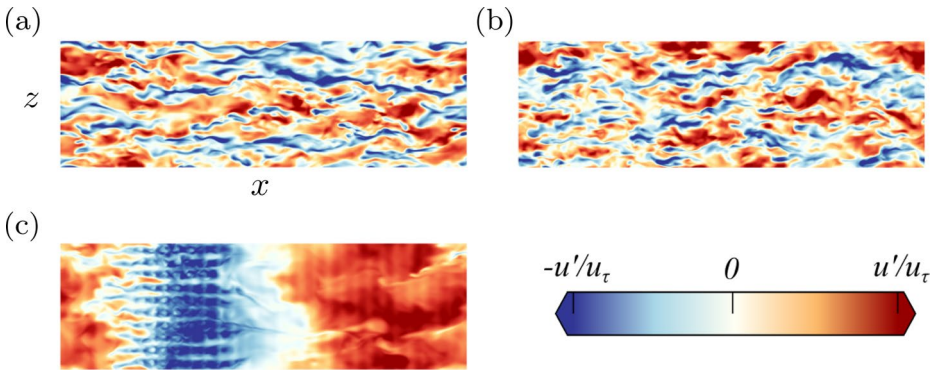



**Fig. 7** Instantaneous slice of streamwise velocity fluctuations $u^{'}$, for (**a**) case S, (**b**) case B, and (**c**) case C, in a wall-parallel plane at $y^+ + l_T^+ = 50$

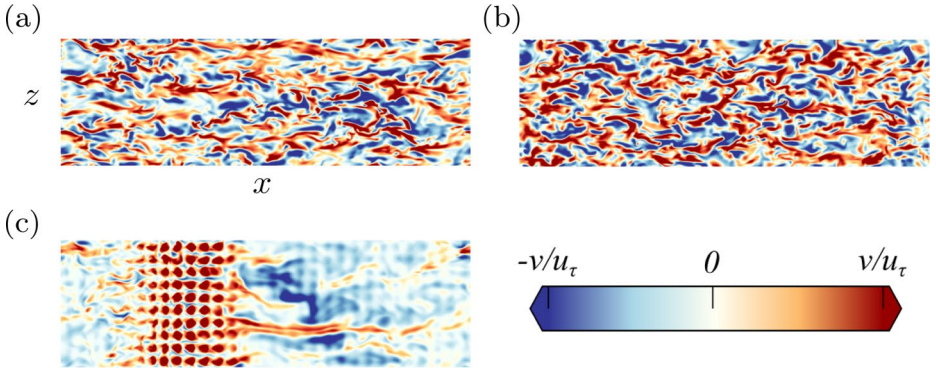



**Fig. 8** Instantaneous slice of wall-normal velocity $v$, for (**a**) case S, (**b**) case B, and (**c**) case C, in a wall-parallel plane at $y^+ + l_T^+ = 50$

wise velocity. It can therefore be hypothesized that these regions are associated with a drag increase that is analyzed and quantified in Sect. 4.1.

The instantaneous flow topology is analyzed by isolating slices in the wall-parallel (as shown in Figs. 7 and 8) and span-normal planes (Fig. 9). The wall-parallel slices are taken at a distance $y^+ + l_T^+ = 50$ as it was identified in Fig. 15 that the wall-bounded flow is no longer dominated by the presence of the porous boundary, as is evidenced by the velocity fluctuation correlation and the pressure gradient of the streamwise momentum budget nearing zero. From Fig. 7, it is apparent that the near-wall flow topology is greatly modified by both the presence of the porous medium and the communication. The magnitudes of the velocity fluctuations are qualitatively similar for all cases. For cases **B** and **C**, the presence of the porous medium leads to the shortening of the streaks (elongated high and low velocity structures in the streamwise direction), with respect to case **S** (Fig. 7(a)). For case **C**, streaks are present but their spanwise spacing is the same as the pore spacing $L_{ref}$. The observations of case **B** are consistent with existing literature on flows over porous media, where the streamwise and spanwise coherence is altered (Shahzad et al. 2023; Kuwata and Suga 2019), while it is different for case **C**, where the presence of communication leads to a

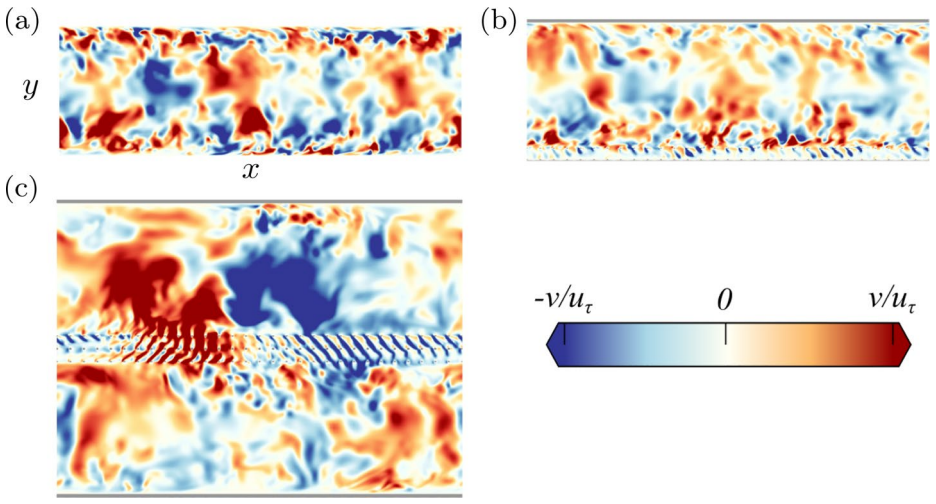



**Fig. 9** Instantaneous slice of wall-normal velocity $v$, for (**a**) case S, (**b**) case B, and (**c**) case C, at the midspan of the simulation

different fully developed regime that is dominated by intermittent slowing of the near-wall cycle. The projection of the pores of the porous medium in the flow features are visible in Fig. 7(c) and not for cases **S** and **B**. The surface topology therefore plays an important role in modifying the near-wall turbulent structures, and the communication process leads to an intermittent slowing of the near-wall cycle.

The modification of the flow is further illustrated by looking at the wall-normal velocity in the same wall-parallel slice, as presented in Fig. 8. Over a smooth wall, as can be seen in Fig. 8(a), the flow topology is dominated by streamwise elongated structures, as well as smaller structures associated with sweep and ejection events (when the streamwise and wall-normal velocity fluctuation are of different signs) (Rajaee et al. 1995; Suga et al. 2018). This differs to case **B**, where wall-normal fluctuations are increased in magnitude, spatial concentration, and smaller in dimensions. It can be reiterated that the porous geometry plays an important role in the spatial distribution of the local injection and ejection events of fluid between the hydrodynamic field in the porous medium and the neighboring wall-bounded flow. Figure 8(c) presents the wall-normal velocity fluctuations for case **C**. The intermittent lower streamwise velocity regions are associated with high wall-normal velocity regions, and can be assimilated to blowing. The regions of high streamwise velocity are associated with injection events where high velocity fluid in the channels is injected in the porous medium. These alternating injection and blowing events are assimilated to wall transpiration, that has also been documented to lead to significant drag increase with this streamwise spacing and convection speed (Quadrio et al. 2007). Comparing the wall-normal and streamwise velocity fields, as shown in Figs. 7 and 8 respectively, the high streamwise velocity is associated with injection of fluid in the porous medium and the lower streamwise velocity is related to the ejection of the low velocity hydrodynamic field present in the porous medium into the channel.

The analysis of the wall-normal velocity in a span-normal slice through the porous medium is shown in Fig. 9. For case **B**, the magnitude of the wall-normal velocity fluctua-

tions is reduced on the opposing smooth wall due to the modification of the friction velocity in the channel. On the porous side, one can observe the flow impinging in the porous medium intermittently, where packets of injection events are observed. This is consistent with observations on acoustic liners (Shahzad et al. 2023). However, Fig. 9(c) shows that the communication extends the modification of the flow to the totality of the channels. The injection and ejection events penetrate through the porous medium, as well as the majority of the wall-bounded flow.

In contrast to the observations in previous literature on porous trailing edges where flow through the porous medium was not documented (Teruna et al. 2021, 2020), Fig. 9(c) shows local flow through. It is possible that the porous trailing edges in Teruna et al. (Teruna et al. 2021, 2020) were not long enough to reach the fully developed regime presented here, since the adaptation length can be expected to be in excess of $10\delta$ (Salomone et al. 2023). Nonetheless, the analysis of the data from Teruna et al. (Teruna et al. 2021), does show that instantaneous flow through the porous medium occurs. For both this study and Teruna et al. (Teruna et al. 2021), this implies that a sufficiently large local pressure gradient across the porous medium is achieved to drive this flow through.

Figure 10(a) shows the spectral density of the wall-normal velocity fluctuations for cases **S**, **B**-LR, **B**-HR, **bB**, and **C**. It is possible to observe that case **C** presents a strong coherence of the signal at 96 Hz, with smaller peaks appearing at the higher harmonics. This does not appear in the other cases. This fundamental frequency corresponds to a Strouhal number, $St = fL/U_b$, of $St_t = 0.02$ based on the thickness of the porous medium and $St_L = 0.22$ based on the coherence length computed in Appendix C. While the Strouhal number based on the porous medium thickness is smaller than the one associated with thick trailing edge shedding (Boldman et al. 1976), it is remarkably close to the range of Strouhal numbers associated with Kelvin-Helmholtz shear instabilities (Michalke 1972). This indicates that the spanwise coherent structures observed are strongly associated with a shear instability

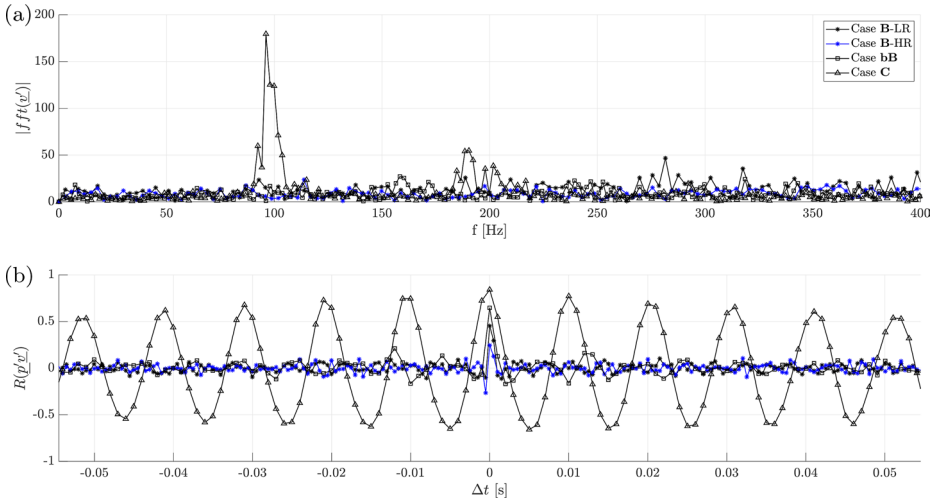



**Fig. 10** (**a**) Normalized wall-normal velocity fluctuations spectral density, and (**b**) pressure differential across the center of the porous medium $y$=0 and $y^+ = 50$ and wall-normal velocity cross correlation for cases B-LR, bB and C at $y^+ + l_T^+ = l_T^+$

due to the shear layer created by the presence of the communication through the porous medium.

The shedding-like behaviour of case **C** is hypothesized to be driven by the pressure differential between the two communicating channels. The cross-correlation of the pressure differential and the wall-normal velocity is computed and shown in Fig. 10(b). In case **C**, the two variables have a 96.5% correlation coefficient meaning that the vast majority of the flow through is driven by the instantaneous wall-normal pressure differential ($\mu_{\Delta p} = 0$, $\sigma_{\Delta p} = 7.8$ Pa, the mean and standard deviation of the pressure differential respectively). While there appears to be intermittent injection events for case **B**-LR, as shown in Fig. 9(b), it is not coherent in time while being pressure driven as the correlation value of 72% at the time lag $\Delta t = 0$s indicates. The spanwise coherent structures described in this section are similar to the ones described in previous studies for grazing flows over porous media (Rosti et al. 2018), flows over canopies (Foggi Rota et al. 2024), and flows over elastic boundaries (Rosti and Brandt 2017). However, the driving mechanism appears to be driven by the anti-symmetric pressure fluctuations between the channels. The correlated pressure fluctuations are related to a mechanism enabled by the permeability of the porous medium (in opposition to its roughness) highlighting a potential decoupling of roughness and permeability effects as was observed in grazing flows (Esteban et al. 2022; Wangsawijaya et al. 2023).

### 3.2 Mean Flow Fields

The mean flow fields are presented in Fig. 11 for a span-normal slice spanning a single unit cell as the solution is spatially periodic. Due to case **S** being homogeneous in wall parallel planes, the analysis is not shown here. This subsection therefore focuses on the results of cases **B** and **C**.

Figure 11(a) presents the velocity fields of case **B**, and Fig. 11(b) for case **C**. These fields correspond to the mean streamwise velocity, the Reynolds streamwise and spanwise stresses, as well as the Reynolds shear stress. In these figures, one can observe that the large open area ratio of the chosen **P075** leads to a significant modification of the velocity field near the porous medium. Comparing cases **B** and **C**, one can observe that the internal hydrodynamic field is convected at a larger velocity in case **C**. It can also be seen that the wall in the mid-plane of the simulation in case **B** leads to the reduction of the unsteady injection of fluid that is observed for case **C**, as shown by the distribution of $\tau_{22}$. It can also be inferred that a larger slip velocity can be achieved in the communicating case. However, a larger pressure drag component can also be expected, due to the interaction between high velocity fluid and the porous geometry. The impact of the drag increase is seen in the top of the figure where a velocity deficit is visible for case **C** with respect to case **B**. The velocity gradient is also decreased as is shown by the increased spacing between the iso-lines of mean velocity in case **C**.

The communication also results in a deeper penetration of the mean flow into the porous medium. To look into more detail into the unsteady interaction in the near-wall region, the mean fluctuating fields are presented in Fig. 11(b). The Reynolds shear stress fields highlight the strong interaction between the streamwise and wall-normal components. The magnitude of the fluctuations is equal or greater than that of the mean streamwise velocity field for case **C**, further corroborating that the flow is dominated by unsteady interactions between

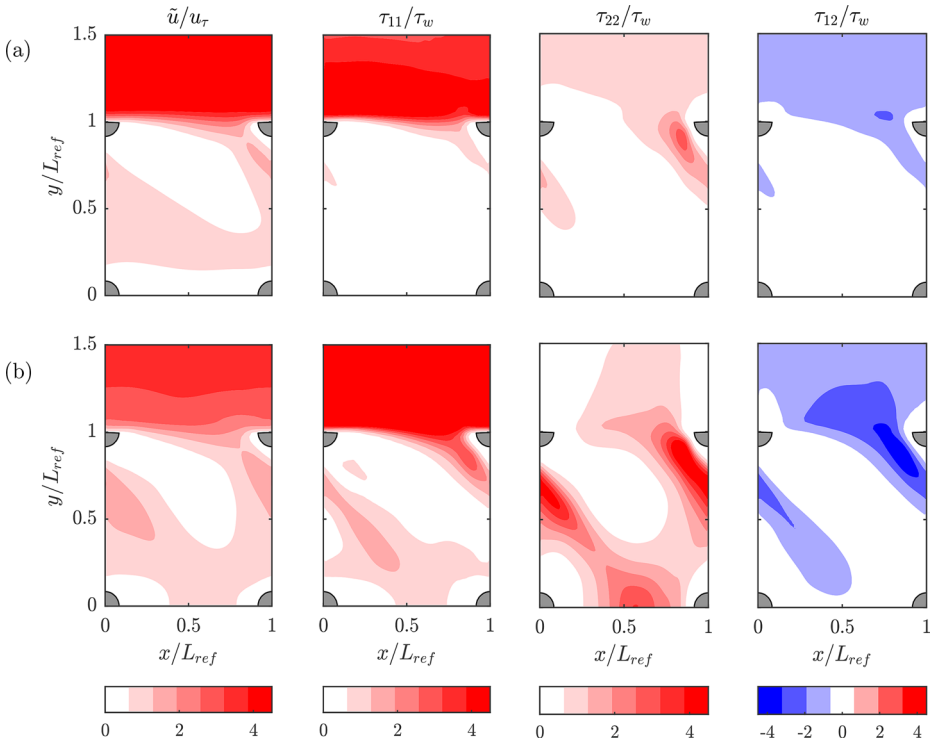



**Fig. 11** Mean slice of viscous-scaled streamwise velocity $\widetilde{u}$ and Reynolds stresses $\tau_{11}$, $\tau_{22}$, $\tau_{12}$ for cases (**a**) B and (**b**) C. The viscous scaling is performed using the friction velocity $u_\tau$, and the wall shear stress $\tau_w$ as described in Sect. 4.1

the communicating grazing flows, and the porous geometry. For case **B**, these interactions are much weaker but present a similar topology. It can be inferred that communication, in facilitating the injection of momentum into the porous geometry, would result in larger inertial effects. The region behind the upstream edge of the porous medium is dominated by the injection of fluid and presents an asymmetry between the injection and ejection of fluid into the grazing flows. This indicates that momentum is lost to inertial effects and friction with the interaction with the porous geometry. Finally, comparing the wall-normal and cross Reynolds stress fields, one can observe that the two stresses are spatially out-of-phase. This indicates that the streamwise velocity is a non-negligible contributor to the injection process as it energizes the fluid being injected in the porous medium. The ejection of slowed down fluid present in the porous medium into the channel can be seen for case **C** with a region of activation of the cross Reynolds stress component.

## 4 Drag Performance and Turbulence Modification

### 4.1 Drag Increase

With the proposed setup, the forcing is constant, therefore the resulting bulk and friction Reynolds numbers are only known *a posteriori*. The drag increase can be quantified using the viscous-scaled velocity deficit (Teruna et al. 2021; Shahzad et al. 2023; Modesti et al. 2021). The viscous scaling can be obtained by computing the equivalent wall shear stress a smooth wall would impart on one of the channels to have the same drag as the porous medium, as illustrated in Fig. 12. In practice, this is done by splitting the force balance between the different channel volumes.

In Fig. 12(a), the typical turbulent channel flow setup shows an equilibrium between the imparted forcing $F$ and the combined friction provided by the wall shear stresses on the top and bottom boundaries $\tau_w$. However, as is highlighted by Fig. 12(b), the equivalent wall shear stress for the communicating case requires to consider each channel separately. Each channel being in equilibrium, the forcing being known a priori, and the friction drag on the wall being measured, the remaining force is attributed to the porous medium, as shown in Fig. 12(c). The wall shear stress is obtained by taking $\tau_{por.,eff.} = (F - \tau_w \times L_x \times L_z)/(L_x \times L_z)$. In this approach, the computed wall-shear stress would correspond to that of a smooth wall of dimension $L_x \times L_z$ with the drag of the porous medium acting on one of the channels at the interface of the channel and the porous medium.

The method of virtual origin is used (Ibrahim et al. 2021; Habibi Khorasani et al. 2022). Its implementation is documented in Appendix D. This step seeks to correct for the penetration of the flow into the porous medium for both cases **B** and **C**. The results are summarised

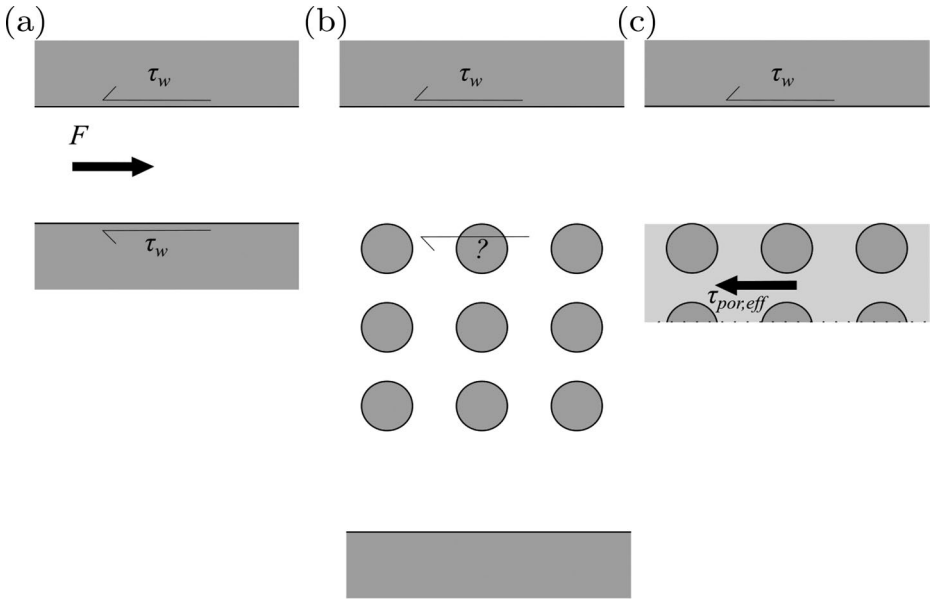



**Fig. 12** Force balance used to determine the equivalent porous wall shear stress. (**a**) the classical turbulent channel flow setup, (**b**) the current setup, and (**c**) the equivalent to the porous medium used to determine the friction velocity

**Table 5** Table summary of the aerodynamic performance of this study's simulations. The convective velocity is taken at $y^+ + l_T^+ = 20$

| Case | $l_T^+$ | $\Delta u^+$ | $u_{\text{conv}}^+$ | Drag $[mN]$ | Drag $[N/m^2]$ | Friction [%] | Pressure [%] | ΔDrag [%] |
|---|---|---|---|---|---|---|---|---|
| Case **S** | 0 | – | 11.6 | 1.09 | 0.910 | 100 | 0 | 0 |
| Case **B**-LR | 6 | 4.09 | 6.95 | 1.43 | 0.397 | 48 | 52 | 63 |
| Case **B**-HR | 6 | 5.51 | 6.94 | 2.78 | 0.771 | 46 | 54 | 93 |
| Case **bB** | 7 | 4.57 | 6.96 | 1.52 | 0.253 | 45 | 55 | 74 |
| Case **C** | 12.5 | 12.1 | 6.81 | 3.70 | 0.595 | 35 | 65 | 626 |

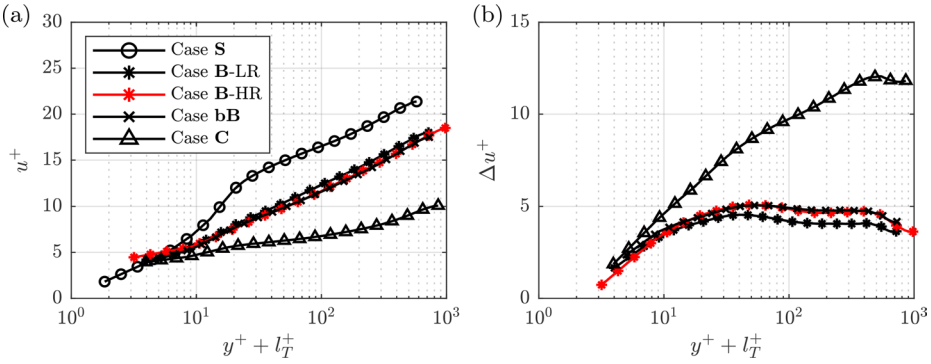



**Fig. 13** Viscous-scaled (**a**) mean velocity and (**b**) velocity deficit profiles comparison

in Table 5. The obtained values for the penetration lengths are larger than previously documented results regarding grazing flows over porous media for case **C**, more than double the largest value reported in Shahzad et al. (Shahzad et al. 2023).

It should be highlighted that the drag increase reported in Table 5 is for a fully developed communicating regime. When considering a porous trailing edge, both boundary layers will adapt spatially to their new communicating condition, and an internal boundary layer is expected to develop (Shahzad et al. 2023) on both sides of the porous trailing edge before reaching the developed regime. Therefore the predicted value represents an upper bound for the additional drag of a porous trailing edge. The velocity deficit, $\Delta u^+$, is used to compute the drag increase with respect to a smooth wall. The relation is given in Eq. 12. In this relation, $u_c^+$ corresponds to the viscous scaled centerline velocity of a smooth wall solution at the same friction Reynolds number $Re_\tau = \frac{\rho_b u_\tau \delta}{\mu}$.

$$\Delta\text{Drag}(\%) = \frac{1}{(1 - \Delta u^+/u_c^+)^2} - 1. \tag{12}$$

The viscous-scaled velocity profiles are presented in Fig. 13. In the velocity profile, the method of virtual origin shift aligns the various parts of the turbulent boundary layer, namely here: the overlap region and the log layer; as seen in Fig. 13(a). In this figure, both the downward shift in velocity profile and the notable difference in shape between cases **B** and **C** are visible. In the region between the overlap region ($5 < y^+ + l_T^+ < 50$) and the log region ($y^+ + l_T^+ > 150$), the gradient of the velocity profile greatly differs for case **C**. In case **B**, the velocity gradient is similar to case **S** and results obtained for grazing flows

over porous media (Wang et al. 2021). In contrast, case **C** appears to display a negligible gradient between $5 < y^+ + l_T^+ < 10$, with a velocity corresponding to the slip velocity. This modification is further explored in Sect. 4.3. The velocity profile of case **C** in the location of the log region indicates a slower velocity recovery in the grazing flow.

The velocity deficit $\Delta u^+$ is obtained by subtracting the velocity profile of cases **B** and **C** with that of a smooth walled solution at the same friction Reynolds number. This results in the profiles shown in Fig. 13(b). In this figure, it is apparent that **C** displays a log-region of reduced extent since it is only present for wall distances in excess of $y^+ + l_T^+ > 300$. The velocity deficit is therefore taken to be the mean $\Delta u^+$ over the interval $y^+ + l_T^+ > 300$ until the centerline. The drag increase values are given in Table 5.

Since the modification of the wall-bounded flow for cases **B**-LR, **B**-HR, and **bB** is extremely similar, and has been extensively documented [Breugem 2005; Suga et al. 2019; Shahzad et al. 2024 ], the subsequent analysis will focus on the differences between case **S**, case **B**-LR (referred to as case **B**), and case **C**.

Two contributions are responsible for the velocity deficit observed. The first is the friction drag. The total friction drag is influenced by both the velocity in the vicinity of the porous surfaces and the increase in surface area with respect to a smooth surface. The second contribution to the additional drag is the pressure drag. The pressure drag contribution is extracted from the decomposition of the force acting on the triangulated surface into its local tangential and normal components. As documented in Table 5, for cases **B** and **C**, the pressure drag is the main contribution to the drag increase. The pressure distribution is expected to also differ due to the presence of the porous medium and will be reflected in the local pressure gradient.

The prevalence of the role of pressure impinging on the porous geometry in the additional drag can be further explored looking at the mean momentum balance in the streamwise direction:

$$\frac{\partial \bar{\rho}\tilde{u}_1\tilde{u}_j}{\partial x_j} + \frac{\partial \bar{\rho}\widetilde{u_1''u_j''}}{\partial x_j} = -\frac{\partial \bar{p}}{\partial x_1} + \frac{\partial \tilde{\sigma}_{1j}}{\partial x_j} + \bar{\Pi}. \tag{13}$$

In this equation, $p$ is the pressure, $\rho$ the density, $u_i$ the velocity along the $i$-th direction, $\sigma$ the viscous diffusion and $\Pi$ the external forcing. The operators $\bar{\bullet}$, and $\tilde{\bullet}$ refer to the Reynolds and Favre averages respectively acting on $\bullet$. Favre averaging was considered due to the weak compressibility of the solution and its impact on turbulence statistics in LBM (Bespalko et al. 2012) and for consistency with previous literature (Shahzad et al. 2023). The fluctuating parts are then defined as $\bullet = \bar{\bullet} + \bullet'$, and $\bullet = \tilde{\bullet} + \bullet''$. It should be noted that for this study, the impact of compressibility is negligible. The verification of the implementation of the budget is shown in Appendix E. Looking at the near-fields of Figure 14 from left to right, the first contribution, that of the Reynolds stress tensor, is much weaker than the others. However the mean gradient of the cross correlation of the streamwise velocity fluctuations with the other velocity fluctuations shows a clear deviation to the smooth case where a monotonic decrease with the wall-distance is expected. For case **B**, the peak value is in a wall parallel plane and can be seen to be located on the downstream edge of the unit-cell. For case **C**, this is enhanced, because the communication allows for the injection of the velocity fluctuations, that in turns increases the interaction with the downstream edge of the unit-cell. Above the porous medium at the downstream edge of the unit-cell, a posi-

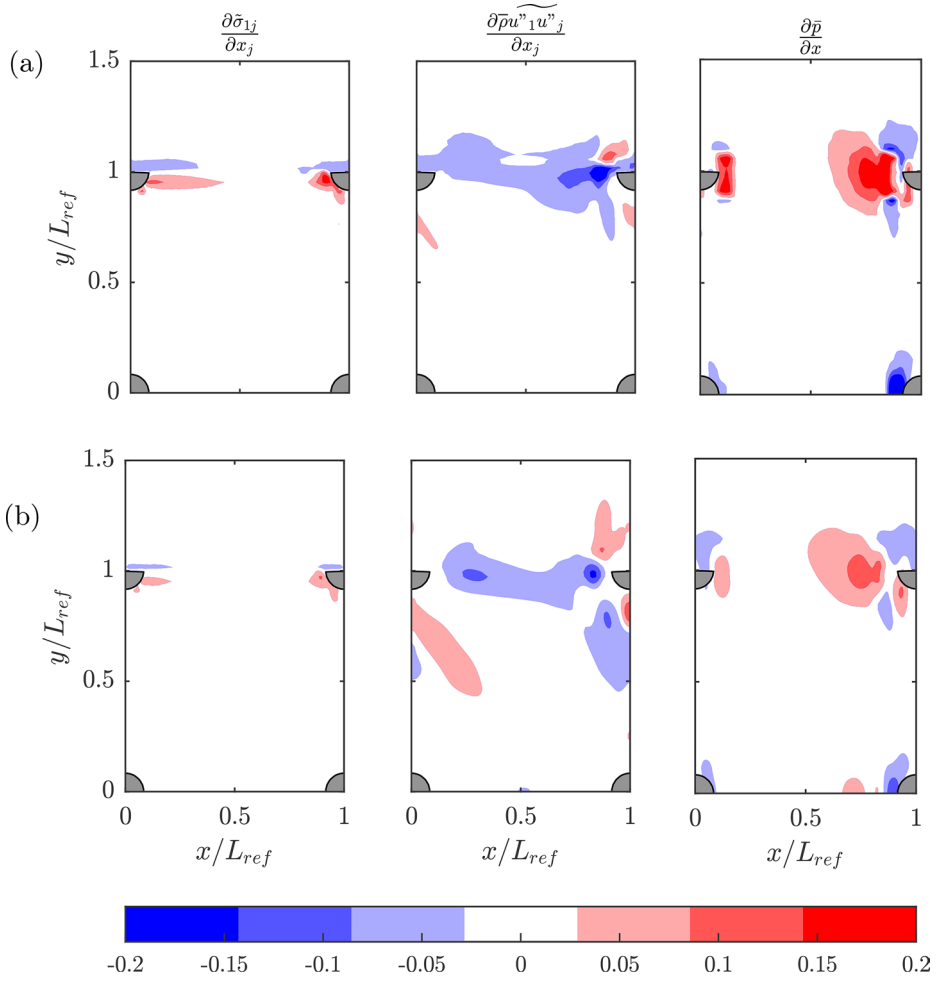



**Fig. 14** Time averaged budget of the streamwise momentum for (**a**) case B and (**b**) case C for a slice in the pore of P075. From left to right, contours of $\frac{\widetilde{\sigma}_{1j}}{\partial x_j}$, $\frac{\partial \widetilde{\bar{\rho} u''_1 u''_j}}{\partial x_j}$, and $\frac{\partial \bar{p}}{\partial x_1}$, with the repeated index $j$ denoting the Einstein notation

tive region is observed for case **C**, where it remains largely negative for case **B**. This means that there is a stronger anti-correlation of the velocity fluctuations further from the porous medium that is not present in case **C**. Finally, the mean pressure gradient appears quite similar for cases **B** and **C** in physical units. Therefore, it can be concluded that while the mean velocity profile is shifted as a function of the virtual origin, the fluctuating properties appear dependent on the physical physical distance to the porous wall. In particular, this dependence highlights the relationship between drag increase and the communicating regime of case **C**, whereas the fluctuating properties are related to the porous topology.

The profiles of the more active terms of the momentum balance are shown in Fig. 15. In this figure, the mean pressure gradient and velocity correlation terms are shown, and high-

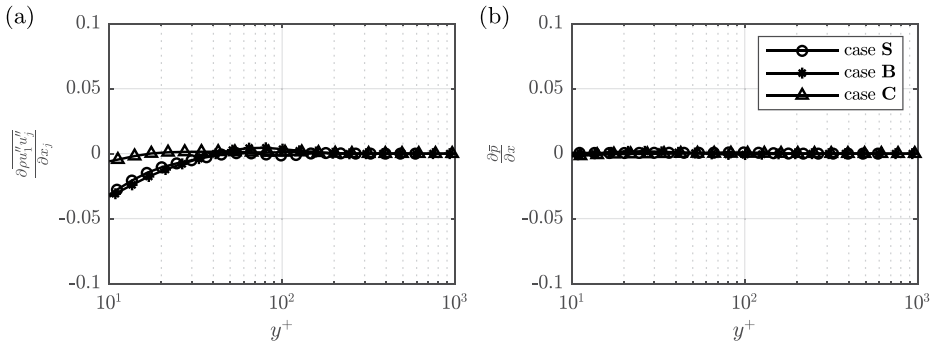



**Fig. 15** Viscous-scaled profiles of the budget of the streamwise momentum for (**a**) the velocity correlation, and (**b**) the streamwise pressure gradient, for cases S (dots), B (stars), and C (triangles)

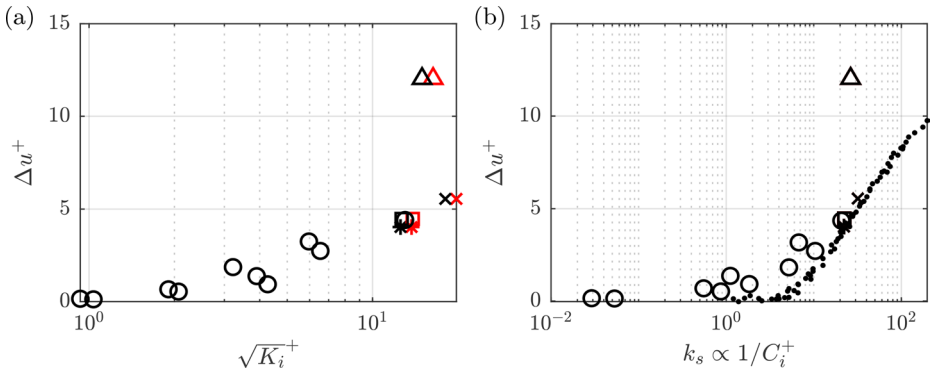



**Fig. 16** Viscous-scaled velocity deficit with respect to material properties. In red, the streamwise material properties ($k_s \approx 0.10/C_x^+$), and black the wall-normal properties ($k_s \approx 0.32/C_y^+$). In dots, the data from (Nikuradse 1950) and circles correspond to the data from (Shahzad et al. 2022)

light the previous observation that the scaling of the flow modifications with wall-distance is conserved (in opposition to viscous-scaled wall coordinates). However, there is a decrease in the peak of the mean velocity correlation gradient for the communicating case. The communication does appear to impact the mean pressure gradient, that is negligible further from the surface $y^+ > 10$.

## 4.2 Relation to Material Properties

Using the material properties described and measured in Sect. 2.5, the relationship between material properties and drag increase can be explored. The velocity deficit can be seen to either relate to the permeability $K$ or the non-linear permeability $C$. Based on this, the plots of Figure 16 are obtained. There is no evident relation between the permeability in either directions $K_x$ or $K_y$ and the drag increase $\Delta u^+$, as illustrated in Fig. 16(a). While case **B** and **bB** appear to correlate with permeability, and in particular wall-normal permeability, case **C** greatly differs from the rest of the data.

The lack of correlation of case **C** with the linear permeability $K_i$ can be explained by the different flow regimes, since communicating wall-bounded flows interact with a bulk surface and the pressure fluctuations on both sides of the porous medium. Moreover, this study finds that porous media with both wall-normal and streamwise permeability collapse with the non-linear permeability and equivalent Hama roughness (Nikuradse 1950), as shows case **B** in Fig. 16(b). Using the same scaling parameter for case **C**, it is evident that the communication leads to a different developed drag increasing regime. Further research looking to determine if the drag increasing regime of the communicating case scales with viscous-scaled non-linear permeability is necessary, which would lead to a different proportionality relationship. This work is beyond the scope of this study, which is looking to characterize the communicating regime.

### 4.3 Turbulence Modification

To further the understanding of the communication mechanisms, and by extension of the pressure release mechanism of porous trailing edges, the modification of the turbulence characteristics is explored. The modification of the energy carrying scales in the boundary layer plays a primordial role in the noise reduction mechanism (Rubio Carpio et al. 2020), as well as the aerodynamic performance (Teruna et al. 2021) of a porous trailing edge. This latter performance can be fully characterized with the present setup.

First, the mean wall shear stress profiles of cases **B** and **C** are given in Fig. 17. Comparing the profiles of the Reynolds stress tensor components of cases **S** and **B**, one can observe that the streamwise fluctuations are decreased due to the presence of the porous medium. The wall-normal and spanwise fluctuating components remain largely unchanged with respect to the smooth wall case **S**. The cross Reynolds shear stress $\tau_{12}$ is also relatively similar, albeit presenting a more significant deficit in the near-wall region.

Case **C** presents similar trends as case **B** for the streamwise and spanwise components. However, the wall-normal and cross Reynolds stress tensor components present high discrepancies with both case **S** and case **B**. This is mainly driven by the modification of the flow topology induced by the shedding-like behaviour of the spanwise coherent turbulent structures. This is analyzed by assessing the budget of the wall-normal velocity variation:

$$\frac{\partial}{\partial x_i}(\bar{\rho}\widetilde{u_2''u_2''}\tilde{u}_i) = P_k + T_k + \Pi_k + \Pi_{\alpha\alpha} - \epsilon, \tag{14}$$

where:

$$\left.\begin{aligned} P_k = -2\bar{\rho}\widetilde{u_2''u_i''}\frac{\partial \bar{u}_2}{\partial x_i}, \quad \epsilon = -2\overline{\sigma_{i2}\frac{\partial u_2''}{\partial x_i}}, \\ T_k = -\frac{\partial}{\partial x_i}\left(\bar{\rho}\widetilde{u_2''u_2''u_i''} - 2\overline{\sigma_{i2}u_2''} + \overline{2p'u_2'}\delta_{2i}\right), \\ \Pi_k = -2\overline{u_2''}\frac{\partial \bar{p}}{\partial y}, \quad \Pi_{\alpha\alpha} = \overline{2p'\frac{\partial u_2'}{\partial y}}. \end{aligned}\right\}$$

In this equation, the mean and fluctuation of the pressure $p$, density $\rho$ and velocities $u$ (in the i-th direction, 1, 2, and 3 being streamwise, wall-normal, and spanwise respectively) are associated into the following terms: the production $P_k$, the dissipation $\epsilon$, the transport $T_k$, the

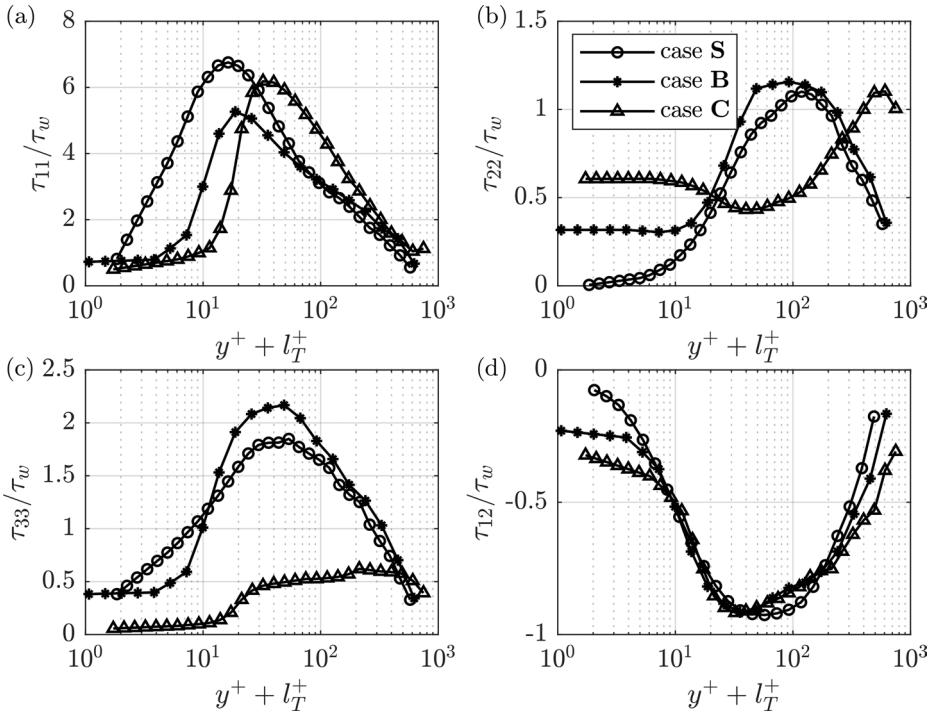



**Fig. 17** Reynolds stress profiles of (**a**) streamwise, (**b**) wall-normal, and (**c**) spanwise velocity fluctuations, (**d**) cross reynolds stress of cases S, B, bB, and C

pressure-velocity correlation $\Pi_k$, and the pressure-strain correlation $\Pi_{\alpha\alpha}$. The verification of the implementation of the budget is shown in Appendix E.

Two results are shown here, first the mean fields through a pore of the **P075** are shown in Fig. 18, and second the mean profiles for the most relevant variables are shown in Fig. 19.

In Fig. 18, one can observe that the main differences between cases **B** and **C** are the transport term $T_k$ and the pressure strain correlation term $\Pi_{\alpha\alpha}$ of the wall-normal velocity variation budget. The first term gives evidence of the role of communication as one can observe that the fluctuations are penetrating much more deeply into the porous medium but also leads to the upwards deflection of the flow at the upstream edge of the porous medium. Additionally, the pressure strain correlation indicates a more fundamental difference in the relation between pressure and velocity fluctuations due to the effect of communication. For case **C**, $\Pi_{\alpha\alpha}$ is no longer dominated by the increase of pressure at the downstream edge of the porous medium but there is a significant negative correlation at the upstream edge of the porous medium. This is due to the shedding-like motion that is observed where the interaction with the geometry not only leads to inertial effects inside the porous medium but also in the wall-bounded flow above. Finally, the production term $P_k$ is active for both cases at the downstream edge of the porous medium, highlighting the role of the porous medium in the turbulence production process. For case **C**, it is associated with additional production from within the porous medium, due to the increased inertial effects of the injection. This is confirmed by the activation of the production term being located where the wall-normal and

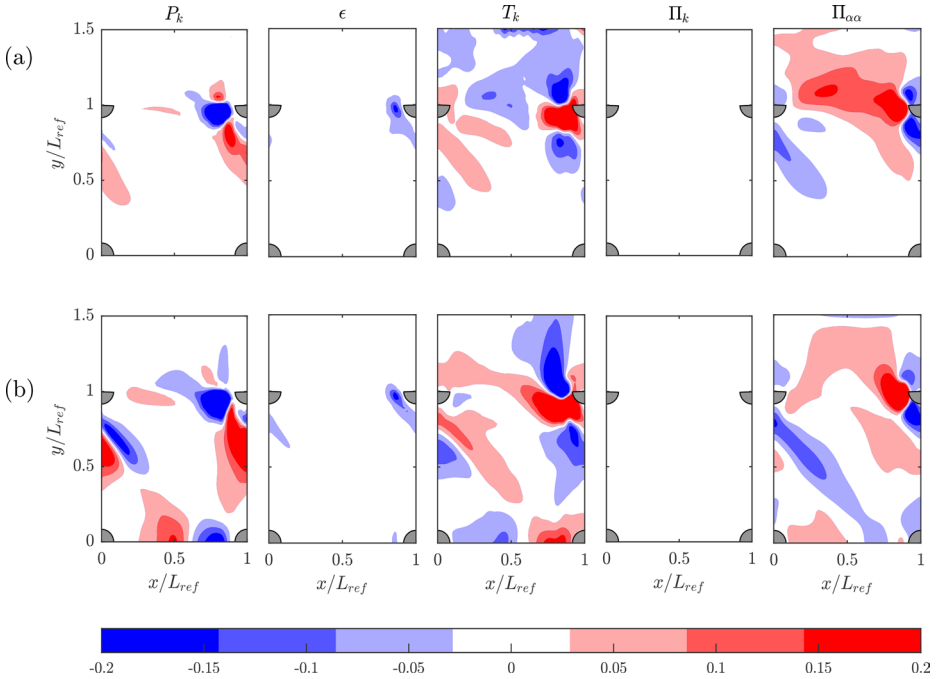



**Fig. 18** Time averaged budget of the wall-normal velocity variation for (**a**) case B and (**b**) case C for a slice in the pore of P075

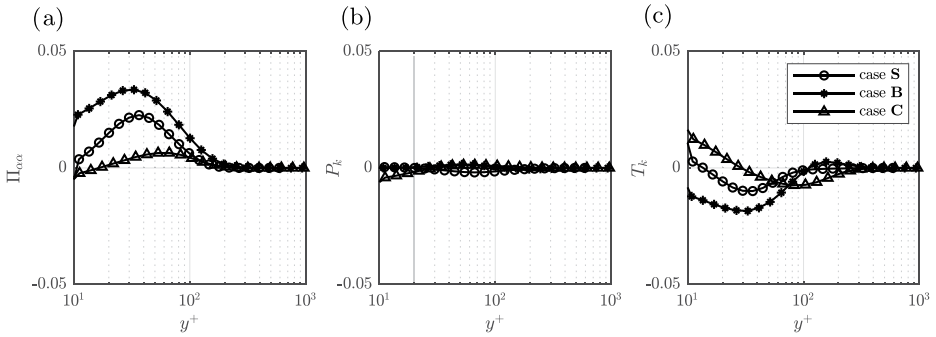



**Fig. 19** Viscous-scaled profiles of the budget of the wall-normal velocity variation for (**a**) the pressure-strain correlation $\Pi_{\alpha\alpha}$, (**b**) the production $P_k$, and (**c**) the transport $T_k$ for cases S (dots), B (stars), and C (triangles)

cross Reynolds stresses are greatest, as shown in Figs. 18 and 12(b) respectively. The production term and the wall-normal dependent Reynolds stresses are both active on the downstream edge of the pore at the fluid/porous interface (cases **B** and **C**) and the downstream edge of the internal porous structure (case **C** only). These locations are both indicative of large velocity fluctuations interacting with the porous geometry itself.

The profiles for the terms $P_k$, $T_K$ and $\Pi_{\alpha\alpha}$ are presented in Fig. 19. The production term is shown to be localized to the near-wall region $y^+ < 10$, as it appears to be zero through-

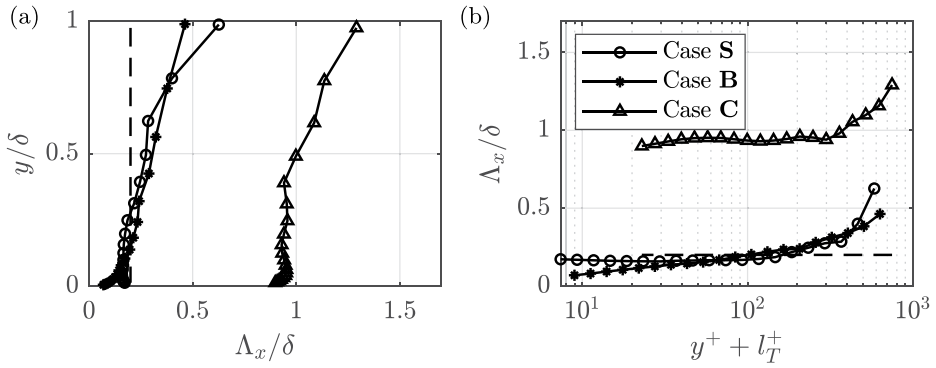



**Fig. 20** Streamwise turbulence integral length scale (**a**) profile and (**b**) viscous-scaled profile for cases S (dots), B (stars), and C (triangles)

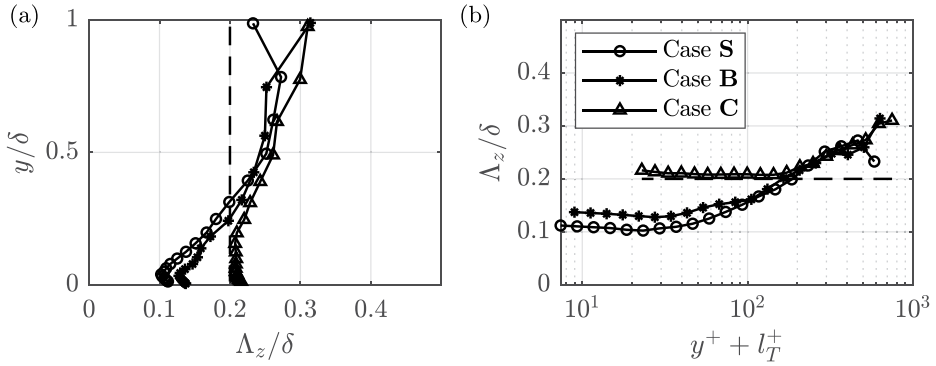



**Fig. 21** Spanwise turbulence integral length scale (**a**) profile and (**b**) viscous-scaled profile for cases S (dots), B (stars), and C (triangles)

out. The transport term and pressure strain correlation are primarily modified in the wall-bounded flow. Cases **B** and **C** appear to have contrasting impacts. The communicating leads to a decrease in the distribution of the pressure strain correlation, falling below that of case **S**. Similarly, the transport term goes from being negative at the porous interface for case **B**, to being positive for case **C**. One can also observe that the transport is most active in the outer layer for case **C**, highlighting the role of the ejection of fluid from the porous medium to the boundary layer.

The integral length scale profiles in the streamwise and spanwise directions are shown in Figs. 20 and 21 respectively. The streamwise integral correlation lengths show that the communication leads to an increase from $0.25\delta$ to $\delta$. While the porous medium leads to a breakdown of the turbulent structures in the near-wall region, as is illustrated by case **B**, the communication has an opposite effect. Moreover, Fig. 20(a) shows that the communication leads to the integral length scale not increasing monotonically with wall distance, as it is constant for a quarter of the channel height.

Additionally, the comparison of the spanwise integral length scale profiles is presented in Fig. 21. In the spanwise direction, the presence of the porous medium in case **B** leads to the

increase of the near-wall spanwise integral length scale. This increase is a result of the near-wall region structures, such as horseshoe vortices, to be limited to having their roots on the underlying porous topology. However, in the log layer of the velocity profile, the difference becomes negligible with the smooth walled case. Additionally, the simultaneous presence of the porous medium and communication leads to the doubling of the turbulence integral length scale near the wall, emphasizing the changes already observed in case **B**. It should be noted that it appears to converge to the value of the pore diameter or $L_{ref}$. Both profiles of cases **S** and **C** converge farther from the wall at approximately $y^+ + l_T^+ \approx 250$ where the velocity profile appears to recover the law of the wall.

For case **C**, despite the increase in magnitude of the wall-normal and cross Reynolds stress components, the main difference occurs in the increase of the streamwise and spanwise integral length scales. It can therefore be inferred that the large wall-normal fluctuations do not dominate the turbulent scales of the flow, unlike the spanwise coherent turbulent structures. In the streamwise direction, the correlation length is approximately $\delta$ which is consistent with the spatio-temporal analysis shown in Appendix C.

Lastly, the turbulence modification induced by the presence of the porous medium (as in case **B**) and by the communication effects (as in case **C**) can also be visualized with the help of spectrograms. Spectrograms give an insight into the organization of turbulence. These are shown in Fig. 22. In (a), (b), and (c), the spectrograms of premultiplied streamwise velocity in the spanwise directions are compared for cases **S**, **B**, and **C** respectively. The organization of the turbulence remains largely similar for cases **S** and **B**. There is a small decrease in the energy carrying scales for scales smaller than $L_{ref}^+$. In case **B**, the larger scales remain largely undisturbed relative to the smaller scales when compared to case **S**. Larger turbulent scales carry more turbulent kinetic energy, with the iso-lines in the figures showing the expected organization with a peak at the near-wall cycle at about $\Lambda_z^+ \approx 100$. For case **B**, it is confirmed that the pore-to-thickness ratio affects the outer-layer similarity as found in Jaiswal and Ganapathisubramani (Jaiswal and Ganapathisubramani 2024). A secondary peak can also be seen in the outer extent of the boundary layer, corresponding to large-scale energetic structures of the outer layer (Marusic et al. 2015). Case **B** does also show additional energy in the scales associated with the porous medium at $\Lambda_z^+ = L_{ref}^+$, with the porous medium facilitating the breakdown of larger structures and accentuating the energy cascade, similar to the results of porous beds (Breugem et al. 2005) and acoustic liners (Shahzad et al. 2023).

Case **C**, as presented in Fig. 22(c), shows more variation from case **S**, and case **B**. The energy is concentrated in the outer layer, where mixing occurs, and at the scale of the unit cell size in the near-wall region. A notable decrease of the inner-cycle energy peak is observed. It corresponds to a drain of the near-wall cycle energy towards scales characterized by the geometry of the porous medium, specifically the pore diameter $d_p$ and the reference length $L_{ref}$(i.e. pore spacing). The outer-cycle peak which is expected at high Reynolds number (Marusic et al. 2015), is partly present. However, in this case, these large scales are dominated by the intermittent streaming (Quadrio et al. 2007), in opposition to the interaction between the inner and outer layers.

The wall-normal velocity spectrogram for case **S**, as shown in Fig. 22(d), and for case **B**, as shown in Fig. 22(e) show that the turbulence structures are similar. The presence

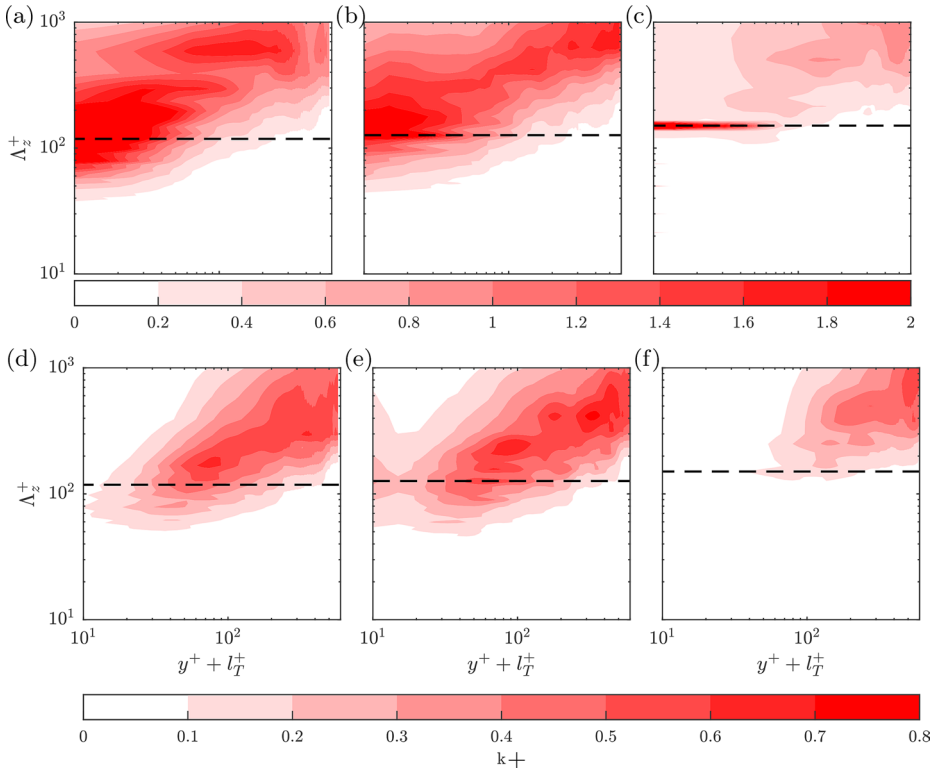



**Fig. 22** Normalized premultiplied velocity spectrograms (**a**), (**b**), (**c**) for the streamwise velocity and (**d**), (**e**), (**f**) for the wall-normal velocity with respect to the local reynolds stress. (**a**), (**d**) show the results of case S, (**b**), (**e**) case B, and (**c**), (**f**) case C. The dotted line corresponds to the pore diameter

of the porous medium in case **B** enhances the mixing and results in a higher turbulence kinetic energy in the near-wall region for scales larger than $\Lambda_z^+ > L_{ref}^+$. However, the lack of energy in the near-wall region for case **C**, as shown in the spectrogram in Fig. 22(f), illustrates a distinct flow topology dominated by the energy in larger scales in the outer layer, namely the spanwise coherent turbulent structures.

The modification of the turbulence organization in case **C** due to the spanwise coherent turbulent structures can also be seen looking at the wall-normal velocity component in Fig. 22(f). In this figure, only the outer peak can be seen with a small amount of energy at the pore spacing scales. This is consistent with the observation of the larger peak no longer resulting from the interaction between the scales but being dominated by the larger spanwise coherent turbulent structure.

The turbulence modification can be seen in more detail in Fig. 23(a) and Fig. 24(a), in the spanwise and streamwise directions respectively. In these slices of near-wall ($y^+ + l_T^+ = 50$) turbulent kinetic energy spectra, the smooth wall case falls between cases **B** and **C**. The porous medium in case **B** is related to an increase in the pressure turbulent kinetic energy, as illustrated in Fig. 23(b) and Fig. 24(b). However, case **C** shows that communication significantly reduces the energy in the pressure fluctuations near the surface, as predicted

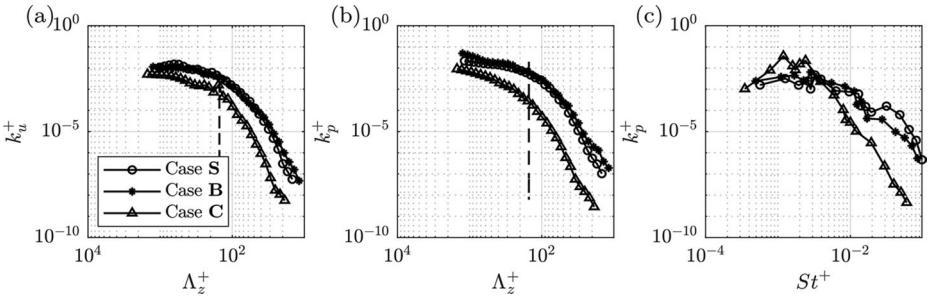



**Fig. 23** (**a**) Normalized turbulent kinetic energy spectrum for the streamwise velocity in the spanwise direction, (**b**) normalized turbulent kinetic energy spectrum for the pressure at $y^+ + l_T^+ = 50$, and (**c**) normalized wall pressure spectrum in the spanwise direction $z$ for cases S, B and C. The cut-off wavelengths in space and time for all cases are $\Lambda_{cut-off}^+ < 4.55$ and $St^+ > 97.3$ respectively, which are beyond the ranges considered here

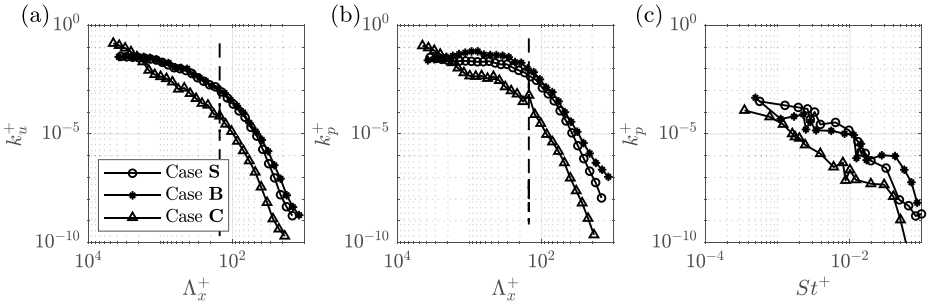



**Fig. 24** (**a**) Normalized turbulent kinetic energy spectrum for the streamwise velocity in the streamwise direction, (**b**) normalized turbulent kinetic energy spectrum for the pressure in the streamwise direction at $y^+ + l_T^+ = 50$, and (**c**) normalized wall pressure spectrum for cases S, B and C

by the pressure release mechanism responsible for the noise reduction of porous trailing edges (Teruna et al. 2021). This decrease in turbulent kinetic energy is reflected in the wall pressure spectrum directly, as presented in Fig. 23(c) and Fig. 24(c). Since the relative order of the spectra for cases **S**, **B**, and **C** are respected and the offset of 2 orders of magnitude between cases **S** and **C** is consistent, the correlation of the spatial turbulence spectra and temporal wall pressure spectrum is high. This indicates that the outer layer could be used to reconstruct the surface pressure fluctuations. This would facilitate the qualitative prediction of the acoustic performance of porous trailing edges from velocity fields.

## 5 Conclusions

In this study, a novel setup was proposed to characterize the interaction, labeled communication, between two wall-bounded flows through a porous medium, as a simplified model of porous trailing edges used for noise mitigation. The numerical setup, solved using the LBM as implemented in PowerFLOW, consisted in two turbulent channel flows communicating

through a pore-resolved porous medium, here the 75% porosity TPMS Schwartz's P. The performance of the communicating setup was compared to that of a smooth walled turbulent channel flow, and an additional control case of a grazing flow over the same porous medium backed by a solid wall.

The existence of a fully developed regime for the communication of turbulent wall-bounded flows through porous media was demonstrated. This regime was characterized by the breakdown of self-similar structures still present in the grazing flow control case. In effect, the flow topology of the communicating regime is dominated by a stronger scale separation. The instantaneous flow fields of the communicating case showed a significant deviation from both the canonical turbulent channel flow and the control cases, with the appearance of stable convected spanwise coherent turbulent structures. These were found to carry the most turbulent kinetic energy in the flow and to be driven by instantaneous pressure fluctuations.

Pressure fluctuations were found to be out-of-phase between the two communicating channels. The organization of the pressure fluctuations led to the instantaneous pressure differential across the porous medium to be sufficient to drive instantaneous flow-through. The wall-normal velocity fluctuations were found to increase within the porous medium as a result. Despite this mechanism, the viscous-scaled wall-normal and spanwise velocity fluctuations were shown to decrease within the log layer, further highlighting the breakdown of the near-wall cycle.

The disruption of the near-wall cycle through the appearance of shedding-like turbulence structures was in turn associated to a large increase in drag in the communicating regime, with respect to both control cases. This finding emphasizes the need to size porous trailing edges accordingly, in order to limit the prevalence of the communicating regime. However, the decrease in kinetic energy for the communicating across most scales further confirms the role of the organization of pressure fluctuations in the pressure release mechanism, responsible for the noise reduction mechanism of porous trailing edges.

Finally, a characterization of the material properties was performed using a pressure drop setup. This highlighted the need to take into account entry and exit effects. Furthermore, it showed that the drag increase of the communicating regime no longer follows the relationship of the grazing flow control case.

Additional studies will be used to determine the relevant non-dimensional groupings in predicting the drag increase in the communicating regime since characteristic length scales fail to capture the relationship between material properties and the aerodynamic performance. The follow up work will also seek to identify an analytical criterion predicting the onset of the communication induced flow modifications. Future work will also seek to explore a wider range of flow conditions and its impact on the communicating regime, with the addition of streamwise pressure gradients and pressure differentials. Lastly, relating the aerodynamic performance to acoustic predictions should be pursued.

**Supplementary Information** The online version contains supplementary material available at https://doi.org/10.1007/s10494-025-00711-1.

**Author Contributions** T.P. Hunter made a major contribution to the conception, the numerical work of this work, the analysis, and the drafting of the work. F. Avallone contributed to the numerical methods. All authors contributed to the interpretation and analysis of the data, as well as reviewed the manuscript.

**Funding** This work used the Dutch national e-infrastructure with the support of the SURF Cooperative using grant no. EINF-8620. The work of F. Avallone is co-funded by the European Union (ERC, LINING, 101075903). Views and opinions expressed are however those of the author(s) only and do not necessarily reflect those of the European Union or the European Research Council. Neither the European Union nor the granting authority can be held responsible for them. All other authors declare that no funding was received for conducting this study, and certify that they have no affiliations with or involvement in any organization or entity with any financial interest or non-financial interest in the subject matter or materials discussed in this manuscript.

**Data Availability** No datasets were generated or analysed during the current study.

## Declarations

**Competing Interests** The authors declare no competing interests.

## References

Aghaei-Jouybari, M., Seo, J.-H., Pinto, S., Cattafesta, L., Meneveau, C., Mittal, R.: Extended Darcy–Forchheimer law including inertial flow deflection effects. J. Fluid. Mech. **980**(13) (2024). https://doi.org/10.1017/jfm.2023.1083

Asbai-Ghoudan, R., Ruiz de Galarreta, S., Rodriguez-Florez, N.: Analytical model for the prediction of permeability of triply periodic minimal surfaces. J. Mech. Behav. Biomed. Mater. **124**, 104804 (2021). https://doi.org/10.1016/j.jmbbm.2021.104804

Avallone, F., Velden, W.C.P., Ragni, D., Casalino, D.: Noise reduction mechanisms of sawtooth and combed-sawtooth trailing-edge serrations. J Fluid Mech. **848**, 560–591 (2018). https://doi.org/10.1017/jfm.2018.377

Baril, E., Mostafid, A., Lefebvre, L.P., Medraj, M.: Experimental demonstration of entrance/exit effects on the permeability measurements of porous materials. Adv. Eng. Mater. **10**(9), 889–894 (2008). https://doi.org/10.1002/adem.200800142

Bespalko, D., Pollard, A., Uddin, M.: Analysis of the pressure fluctuations from an LBM simulation of turbulent channel flow. Comput. & Fluids. **54**(1), 143–146 (2012). https://doi.org/10.1016/j.compfluid.2011.10.008

Bhatnagar, P.L., Gross, E.P., Krook, M.: A Model for collision processes in gases. I. Small amplitude processes in charged and neutral one-component Systems. Phys. Rev. E. **94**(3), 511–525 (1954). https://doi.org/10.1103/PhysRev.94.511

Boldman, D.R., Brinich, P.F., Goldstein, M.E.: Vortex shedding from a blunt trailing edge with equal and unequal external mean velocities. J. Fluid. Mech. **75**(4), 721–735 (1976). https://doi.org/10.1017/S0022112076000499

Breugem, W.P.: The Influence of Wall Permeability on Laminar and Turbulent Flows. PhD thesis, 2005, Delft University of Technology

Breugem, W.P., Boersma, B.J., Uittenbogaard, R.E.: The laminar boundary layer over a permeable wall. Transp. In Porous Media **59**(3), 267–300 (2005). https://doi.org/10.1007/s11242-004-2557-1

Brooks, T.F., Pope, D.S., Marcolini, M.A.: Airfoil self-noise and prediction. NASA Reference Publication (1218) (1989)

Chen, H., Chen, S., Matthaeus, W.H.: Recovery of the Navier-Stokes equations using a lattice-gas Boltzmann method. Phys. Rev., A **45**(8), 5339–5342 (1992). https://doi.org/10.1103/PhysRevA.45.R5339

Chen, H., Orszag, S.A., Staroselsky, I., Succi, S.: Expanded analogy between Boltzmann kinetic theory of fluids and turbulence. J. Fluid. Mech. **519**, 301–314 (2004). https://doi.org/10.1017/S0022112004001211

Chen, H., Teixeira, C., Molvig, K.: Realization of fluid boundary conditions via discrete Boltzmann dynamics. Int. J. Mod. Phys. C. **9**(8), 1281–1292 (1998). https://doi.org/10.1142/S0129183198001151

Esteban, L.B., Rodríguez-López, E., Ferreira, M.A., Ganapathisubramani, B.: Mean flow of turbulent boundary layers over porous substrates. Phys. Rev. Fluids. **7**(9), 1–16 (2022). https://doi.org/10.1103/PhysRevFluids.7.094603

Feng, J., Liu, B., Lin, Z., Fu, J.: Isotropic porous structure design methods based on triply periodic minimal surfaces. Mater. Des. **210**, 110050 (2021). https://doi.org/10.1016/j.matdes.2021.110050

Foggi Rota, G., Monti, A., Olivieri, S., Rosti, M.E.: Dynamics and fluid-structure interaction in turbulent flows within and above flexible canopies. J. Fluid. Mech. **989**, 1–34 (2024). https://doi.org/10.1017/jfm.2024.481

Gandy, P.J.F., Bardhan, S., Mackay, A.L., Klinowski, J.: Nodal surface approximations to the P, g, D and I-WP triply periodic minimal surfaces. Chem. Phys Lett. **336**(3–4), 187–195 (2001). https://doi.org/10.1016/S0009-2614(00)01418-4

Gandy, P.J.F., Klinowski, J.: Exact computation of the triply periodic Schwarz P ('primitive') minimal surface. Chem. Phys. Lett. **321**(5–6), 363–371 (2000). https://doi.org/10.1016/S0009-2614(00)00373-0

Geyer, T., Sarradj, E., Fritzsche, C.: Porous airfoils: noise reduction and boundary layer effects. 15th AIAA/CEAS Aeroacoustics Conference (30th AIAA Aeroacoustics Conference) **9**(6), 787–820 (2009). https://doi.org/10.2514/6.2009-3392

Habibi Khorasani, S.M., Lācis, U., Pasche, S., Rosti, M.E., Bagheri, S.: Near-wall turbulence alteration with the transpiration-resistance model. J. Fluid. Mech. **942**(45) (2022). https://doi.org/10.1017/jfm.2022.358. arXiv:2105.09391

Herr, M., Rossignol, K.S., Delfs, J.W., Mößner, M., Lippitz, N.: Specification of porous materials for low-noise trailing-edge applications. In: 20th AIAA/CEAS Aeroacoustics Conference (June), pp. 1–19. (2014). https://doi.org/10.2514/6.2014-3041

Ibrahim, J.I., Gómez-de-Segura, G., Chung, D., García-Mayoral, R.: The smooth-wall-like behaviour of turbulence over drag-altering surfaces: a unifying virtual-origin framework. J. Fluid. Mech. **915**(56) (2021). https://doi.org/10.1017/jfm.2021.13 arXiv:2006.16118

Jaiswal, P., Ganapathisubramani, B.: Effects of porous substrates on the structure of turbulent boundary layers. J. Fluid. Mech. **980**, 1–29 (2024). https://doi.org/10.1017/jfm.2024.45

Jones, L.E., Sandberg, R.D.: Acoustic and hydrodynamic analysis of the flow around an aerofoil with trailing-edge serrations. J. Fluid. Mech. **706**, 295–322 (2012). https://doi.org/10.1017/jfm.2012.254

Kuwata, Y., Suga, K.: Extensive investigation of the influence of wall permeability on turbulence. Int. J. Heat. Fluid. Flow **80**(September), 108465 (2019). https://doi.org/10.1016/j.ijheatfluidflow.2019.108465

Launder, B.E., Spalding, D.B.: Numerical prediction of flow, heat transfer, turbulence and combustion. Elsevier 96–116 (1983). https://doi.org/10.1016/B978-0-08-030937-8.50016-7

Lee, S., Ayton, L.J., Bertagnolio, F., Moreau, S., Chong, T.P., Joseph, P.F.: Turbulent boundary layer trailing-edge noise: theory, computation, experiment, and application. Prog. Aerosp. Sci. **126**(May), 100737 (2021). https://doi.org/10.1016/j.paerosci.2021.100737

Luesutthiviboon, S., Ragni, D., Avallone, F., Snellen, M.: An alternative permeable topology design space for trailing-edge noise attenuation. Int. J. Multiling. Aeroacoust. **20**(3–4), 221–253 (2021). https://doi.org/10.1177/1475472X211003295

Marcus, H.: The permeability of a sample of an anisotropic porous medium. J. Geophys. Res.: Earth Surf. **67**(13), 5215–5225 (1962). https://doi.org/10.1029/JZ067i013p05215

Marusic, I., Chauhan, K.A., Kulandaivelu, V., Hutchins, N.: Evolution of zero-pressure-gradient boundary layers from different tripping conditions. J. Fluid. Mech. **783**, 379–411 (2015). https://doi.org/10.1017/jfm.2015.556

Meeks, W.H., III: The theory of triply periodic minimal surfaces. Indiana Univ. Math. J. **39**(3), 877–936 (1990)

Michalke, A.: The instability of free shear layers. Prog. Aerosp. Sci. **12**(C), 213–216 (1972). https://doi.org/10.1016/0376-0421(72)90005-X

Modesti, D., Endrikat, S., Hutchins, N., Chung, D.: Dispersive stresses in turbulent flow over riblets. J. Fluid. Mech. **917** (2021). https://doi.org/10.1017/jfm.2021.310

Nikuradse, J.: Laws of flow in rough pipes. NACA Technical Report. **5**, 738–757 (1950). https://doi.org/10.1051/lhb/1951058

Piest, B.J.T., Druetta, P.D., Krushynska, A.O.: Mitigation of flow-induced vibrations in high-speed flows using triply periodic minimal surface structures. Phys. of Fluids. **36**(10) (2024). https://doi.org/10.1063/5.0225526

Pope, S.B.: Turbulent flows., pp. 93–130. Cambridge University Press (2000). https://doi.org/10.1017/CBO9780511840531

Quadrio, M., Floryan, J.M., Luchini, P.: Effect of streamwise-periodic wall transpiration on turbulent friction drag. J Fluid Mech. **576**, 425–444 (2007). https://doi.org/10.1017/S0022112007004727

Rajaee, M., Karlsson, S., Sirovich, L.: On the streak spacing and vortex roll size in a turbulent channel flow. Phys. Of Fluids **7**(10), 2439–2443 (1995). https://doi.org/10.1063/1.868688

Rosti, M.E., Brandt, L.: Numerical simulation of turbulent channel flow over a viscous hyper-elastic wall. J Fluid Mech. **830**, 708–735 (2017). https://doi.org/10.1017/jfm.2017.617 arXiv:1705.08822

Rosti, M.E., Brandt, L., Pinelli, A.: Turbulent channel flow over an anisotropic porous wall – drag increase and reduction. J Fluid Mech. **842**, 381–394 (2018). https://doi.org/10.1017/jfm.2018.152

Rubio Carpio, A., Avallone, F., Ragni, D., Snellen, M., Zwaag, S.: Quantitative criteria to design optimal permeable trailing edges for noise abatement. J. Sound Vib. **485**, 115596 (2020). https://doi.org/10.1016/j.jsv.2020.115596

Rubio Carpio, A., Merino Martínez, R., Avallone, F., Ragni, D., Snellen, M., Zwaag, S.: Experimental characterization of the turbulent boundary layer over a porous trailing edge for noise abatement. J. Sound Vib. **443**, 537–558 (2019). https://doi.org/10.1016/j.jsv.2018.12.010

Salomone, T., Piomelli, U., De Stefano, G.: Wall-modeled and hybrid large-eddy simulations of the flow over roughness strips. Fluids **8**(1), 1–16 (2023). https://doi.org/10.3390/fluids8010010

Nodal surfaces of fourier series: fundamental invariants of structured matter. Z. für Phys. B Condens. Matter **83**(3), 407–412 (1991). https://doi.org/10.1007/BF01313411.Schnering H.G., Nesper, R.

Shahzad, H., Hickel, S., Modesti, D.: Permeability and turbulence over perforated plates. Flow Turbul. Combust. **109**(4), 1241–1254 (2022). https://doi.org/10.1007/s10494-022-00337-7 arXiv:2203.04753

Shahzad, H., Hickel, S., Modesti, D.: Turbulence and added drag over acoustic liners. J Fluid Mech. **965**(10) (2023). https://doi.org/10.1017/jfm.2023.397. arXiv:2210.17354

Shahzad, H., Hickel, S., Modesti, D.: Physics-informed acoustic Liner optimization: balancing drag and noise. Aiaa J. **1–9** (2024). https://doi.org/10.2514/1.J063677

Suga, K., Okazaki, Y., Ho, U., Kuwata, Y.: Anisotropic wall permeability effects on turbulent channel flows. J Fluid Mech. **855**, 983–1016 (2018). https://doi.org/10.1017/jfm.2018.666

Suga, K., Okazaki, Y., Matsuo, T., Taneo, A., Kuwata, Y.: Measurement of turbulent square duct flows over anisotropic porous media. In: 11th International Symposium on Turbulence and Shear Flow Phenomena, TSFP 2019. (2019)

Teixeira, C.M.: Incorporating turbulence models into the lattice-Boltzmann Method. Int. J. Mod. Phys. C. **9**(8), 1159–1175 (1998). https://doi.org/10.1142/S0129183198001060

Teruna, C., Avallone, F., Casalino, D., Ragni, D.: Numerical investigation of leading edge noise reduction on a rod-airfoil configuration using porous materials and serrations. J. Sound Vib. **494**, 1–25 (2021). https://doi.org/10.1016/j.jsv.2020.115880

Teruna, C., Avallone, F., Ragni, D., Casalino, D.: On the noise reduction of a porous trailing edge applied to an airfoil at lifting condition. Phys. Of Fluids **33**(5), 1 (2021). https://doi.org/10.1063/5.0047512

Teruna, C., Avallone, F., Ragni, D., Rubio Carpio, A., Casalino, D.: Numerical analysis of a 3-D printed porous trailing edge for broadband noise reduction. J Fluid Mech. **926**, 1–36 (2021). https://doi.org/10.1017/jfm.2021.704

Teruna, C., Manegar, F.A., Avallone, F., Ragni, D., Casalino, D., Carolus, T.: Noise reduction mechanisms of an open-cell metal-foam trailing edge. J Fluid Mech. **898** (2020). https://doi.org/10.1017/jfm.2020.363

Teruna, C., Rego, L., Avallone, F., Ragni, D., Casalino, D.: Applications of the multilayer porous medium modeling approach for noise mitigation. J Aerosp Eng. **34**(6), 04021074 (2021). https://doi.org/10.1061/(asce)as.1943-5525.0001326

Tjaden, B., Brett, D.J.L., Shearing, P.R.: Tortuosity in electrochemical devices: a review of calculation approaches. Int. Mater. Rev. **63**(2), 47–67 (2018). https://doi.org/10.1080/09506608.2016.1249995

Wang, W., Chu, X., Lozano-Durán, A., Helmig, R., Weigand, B.: Information transfer between turbulent boundary layers and porous media. J Fluid Mech. **920**, 1–10 (2021). https://doi.org/10.1017/jfm.2021.445 arXiv:2011.01305

Wangsawijaya, D.D., Jaiswal, P., Ganapathisubramani, B.: Towards decoupling the effects of permeability and roughness on turbulent boundary layers. J Fluid Mech. **967** (2023). https://doi.org/10.1017/jfm.2023.497

Wilcox, D.C.: Turbulence modeling for cfd. DCW industries (v. **1** (2006)

Ye, Q., Avallone, F., Ragni, D., Choudhari, M., Casalino, D.: Effect of surface roughness on boundary layer transition and far field noise. In: 25th AIAA/CEAS Aeroacoustics Conference, pp. 2019. (2019). https://doi.org/10.2514/6.2019-2551

Zhou, P., Zhong, S., Li, X., Li, Y., Chen, W., Jiang, H., Zhang, X.: Broadband trailing edge noise reduction through porous velvet-coated serrations. Phys. Fluids **34**(5) (2022). https://doi.org/10.1063/5.0089257

**Publisher's Note** Springer Nature remains neutral with regard to jurisdictional claims in published maps and institutional affiliations.

Springer Nature or its licensor (e.g. a society or other partner) holds exclusive rights to this article under a publishing agreement with the author(s) or other rightsholder(s); author self-archiving of the accepted manuscript version of this article is solely governed by the terms of such publishing agreement and applicable law.

## Authors and Affiliations

**Thomas P. Hunter[1] · Francesco Avallone[2] · Nguyen Anh Khoa Doan[1] · Daniele Ragni[1]**

✉ Thomas P. Hunter
t.p.hunter@tudelft.nl

Francesco Avallone
francesco.avallone@polito.it

Nguyen Anh Khoa Doan
n.a.k.doan@tudelft.nl

Daniele Ragni
d.ragni@tudelft.nl

[1] FPT Department, Faculty of Aerospace Engineering, Delft University of Technology, Kluyverweg 2, Delft 2629HS, The Netherlands

[2] DIMEAS, Politecnico di Torino, Corso Duca degli Abruzzi 24, 10129 Torino, Italy